Monthly Notices of the ROYAL ASTRONOMICAL SOCIETY

MNRAS **544,** 1710–1731 (2025) https://doi.org/10.1093/mnras/staf1857
Advance Access publication 2025 October 29

MIGHTEE-H I: the $M_{\rm H\,I} - M_\star$ relation of massive galaxies and the H I mass function at $0.25 < z < 0.5$

Hengxing Pan [1,2,3★] Matt J. Jarvis [3,4] Ian Heywood [3,5,6] Tariq Yasin [3] Natasha Maddox [7] Mario G. Santos [4,6] Maarten Baes [8] Anastasia A. Ponomareva [3,9] and Sambatriniaina H. A. Rajohnson [10]

[1]*National Astronomical Observatories, Chinese Academy of Sciences, Beijing 100101, P. R. China*
[2]*Guizhou Radio Astronomical Observatory, Guizhou University, Guiyang 550000, China*
[3]*Astrophysics, University of Oxford, Denys Wilkinson Building, Keble Road, Oxford OX1 3RH, UK*
[4]*Department of Physics and Astronomy, University of the Western Cape, Cape Town 7535, South Africa*
[5]*Centre for Radio Astronomy Techniques and Technologies, Department of Physics and Electronics, Rhodes University, PO Box 94, Makhanda 6140, South Africa*
[6]*South African Radio Astronomy Observatory (SARAO), 2 Fir Street, Observatory 7925, South Africa*
[7]*School of Physics, H.H. Wills Physics Laboratory, Tyndall Avenue, University of Bristol, Bristol BS8 1TL, UK*
[8]*Sterrenkundig Observatorium, Universiteit Gent, Krijgslaan 281 S9, B-9000 Gent, Belgium*
[9]*Centre for Astrophysics Research, School of Physics, Astronomy and Mathematics, University of Hertfordshire, College Lane, Hatfield AL10 9AB, UK*
[10]*INAF – Osservatorio Astronomico di Cagliari, Via della Scienza 5, I-09047 Selargius (CA), Italy*

Accepted 2025 October 24. Received 2025 October 24; in original form 2025 February 11

ABSTRACT

The relationship between the already formed stellar mass in a galaxy and the gas reservoir of neutral atomic hydrogen, is a key element in our understanding of how gas is turned into stars in galaxy haloes. In this paper, we measure the $M_{\rm H\,I} - M_\star$ relation based on a stellar-mass selected sample at $0.25 < z < 0.5$ and the MeerKAT International GHz Tiered Extragalactic Exploration-H I Data Release 1 spectral data. Using a powerful Bayesian stacking technique, for the first time we are also able to measure the underlying bivariate distribution of H I mass and stellar mass of galaxies with $M_\star > 10^{9.5}\,{\rm M}_\odot$, finding that an asymmetric underlying H I distribution is strongly preferred by our complete samples. We define the concepts of the average of the logarithmic H I mass, $\langle \log_{10}(M_{\rm H\,I})\rangle$, and the logarithmic average of the H I mass, $\log_{10}(\langle M_{\rm H\,I}\rangle)$, and find that the difference between $\langle \log_{10}(M_{\rm H\,I})\rangle$ and $\log_{10}(\langle M_{\rm H\,I}\rangle)$ can be as large as ∼0.5 dex for the preferred asymmetric H I distribution. We observe shallow slopes in the underlying $M_{\rm H\,I} - M_\star$ scaling relations, suggesting the presence of an upper H I mass limit beyond which a galaxy can no longer retain further H I gas. From our bivariate distribution we also infer the H I mass function at this redshift and find tentative evidence for a decrease of 2–10 times in the comoving space density of the most H I massive galaxies up to $z \sim 0.5$.

Key words: methods: statistical – galaxies: fundamental parameters – radio lines: galaxies.

1 INTRODUCTION

Neutral atomic hydrogen (H I) gas serves as the raw fuel for star formation in galaxies. The relationship between neutral atomic hydrogen gas and stars provides insight into a galaxy's evolutionary stage. However, the relationship between H I and stellar mass ($M_{\rm H\,I} - M_\star$) is complex because of the intricate physical processes involved in galaxy evolution. Consequently, a simple correlation describing the $M_{\rm H\,I} - M_\star$ relation is insufficient to capture the full complexity of this relation. Gaining a deeper understanding of this relation is crucial for uncovering the mechanisms that drive galaxy evolution from youth to maturity (e.g. A. Rodríguez-Puebla et al. 2020; A. Saintonge & B. Catinella 2022).

In particular, N. Maddox et al. (2015) and H. Pan et al. (2024) explored the upper envelope of the H I and stellar mass ($M_{\rm H\,I} - M_\star$) relation based on H I selected samples from Arecibo Legacy Fast ALFA (ALFALFA), MeerKAT International GHz Tiered Extragalactic Exploration (MIGHTEE), and FAST COSMOS H I surveys, enlightening the processes of gas consumption and star formation. In complementary studies, B. Catinella et al. (2010) and V. Parkash et al. (2018) explored the underlying $M_{\rm H\,I} - M_\star$ relation based on stellar mass-selected samples, highlighting the role of gas poor early-type galaxies in regulating the intrinsic $M_{\rm H\,I} - M_\star$ relation.

The direct detection of emission lines from the neutral hydrogen component of galaxies has been limited to the local Universe or massive H I systems, constrained by the sensitivity of modern radio instruments such as the Parkes and Arecibo telescopes in the past few decades. Despite these limitations, several H I studies have been carried out from the H I Parkes All-Sky Survey (D. G. Barnes et al. 2001), the ALFALFA survey (R. Giovanelli et al. 2005), to the more

★ E-mail: panhengxing@nao.cas.cn

recent, MIGHTEE (M. Jarvis et al. 2016) survey, Looking at the Distant Universe with the MeerKAT Array (S. Blyth et al. 2016), and the FAST All Sky H I survey (C.-P. Zhang et al. 2024) using MeerKAT (J. Jonas & MeerKAT Team 2016) and the Five-hundred-meter Aperture Spherical Radio Telescope (FAST; R. Nan et al. 2011), respectively.

At higher redshift ($z > 0.1$), the number of direct detections from H I surveys is limited due to the faintness of the 21-cm line, with only recent surveys gradually building up larger samples (e.g. H. Xi et al. 2024; M. J. Jarvis et al. 2025), thus H I studies tend to rely on statistical approaches. The straightforward way is to average the H I fluxes at known locations of sources detected in other wavelengths, thus increasing the signal-to-noise ratio using the stacking technique (e.g. J. Delhaize et al. 2013; J. Healy et al. 2019; F. Sinigaglia et al. 2022). However, a simple averaging in the flux space risks losing information on the intrinsic scatter of H I distribution (or shape of H I mass function, see e.g. A. Bera et al. 2022; F. Sinigaglia et al. 2025), limiting the accessible knowledge of the $M_{\rm H\,I} - M_\star$ relation from the noisy H I data at high redshifts. The underlying H I mass distribution as a function of the stellar mass reveals how strong the H I mass correlates with the stellar mass and hence traces the conversion of gas into stars, which is crucial for constraining the evolutionary stage of galaxies, and inferring the total amount of H I gas by linking to the H I mass function (e.g. A. A. Ponomareva et al. 2023; A. Kazemi-Moridani et al. 2024).

In this paper, we implement a Bayesian stacking technique, based on our previous work (H. Pan et al. 2021, 2023), for measuring the underlying $M_{\rm H\,I} - M_\star$ scaling relation by combining the MIGHTEE Data Release (DR1) H I images and an optical catalogue at $0.25 < z < 0.5$, while taking into account the intrinsic H I scatter as a function of the stellar mass. This technique employs fluxes of H I emission line as measurables while modelling the underlying H I mass distribution that can naturally account for the thermal noise scatter from the radio receiver on the linear flux scale, and the intrinsic H I scatter on the logarithmic mass scale.

This paper is organized as follows: We describe our MIGHTEE-H I and the ancillary data in Section 2, and the Bayesian technique in Section 3. We present our main results in Section 4, and conclude in Section 5. We use the standard ΛCDM cosmology with a Hubble constant $H_0 = 70\,{\rm km\,s^{-1}\,Mpc^{-1}}$, total matter density $\Omega_{\rm m} = 0.3$ and dark energy density $\Omega_\Lambda = 0.7$, and AB magnitudes throughout when magnitudes are used.

2 DATA

2.1 MIGHTEE-H I

MIGHTEE-H I is the H I emission project within the MIGHTEE survey. The MIGHTEE Early Science (E.S.) data were collected between mid-2018 and mid-2019 and are described by N. Maddox et al. (2021) in detail. For this study, we use the latest MIGHTEE Data Release 1, observed with the 32k channel mode of the MeerKAT telescope (I. Heywood et al. 2024) across the *L* band. The MeerKAT 32k correlator mode provides 32 768 channels with a spectral resolution of 26.1 kHz, corresponding to 5.5 km s^{-1} at 1420 MHz. The *L* band has been split into two sub-bands (*L 1* and *L 2*) with the frequency ranges of these sub-bands are 960–1150 MHz ($0.23 < z_{\rm H\,I} < 0.48$) and 1290–1520 MHz ($0 < z_{\rm H\,I} < 0.1$), respectively. Note that the *L1* band cube has a velocity resolution of 27.6 km s^{-1} for H I at $z = 0.25$, and we round the H I redshift range of *L1* band as $0.25 < z < 0.5$ hereafter. The COSMOS field was observed using this mode with 15 × 8h tracks, arranged in a tightly dithered mosaic

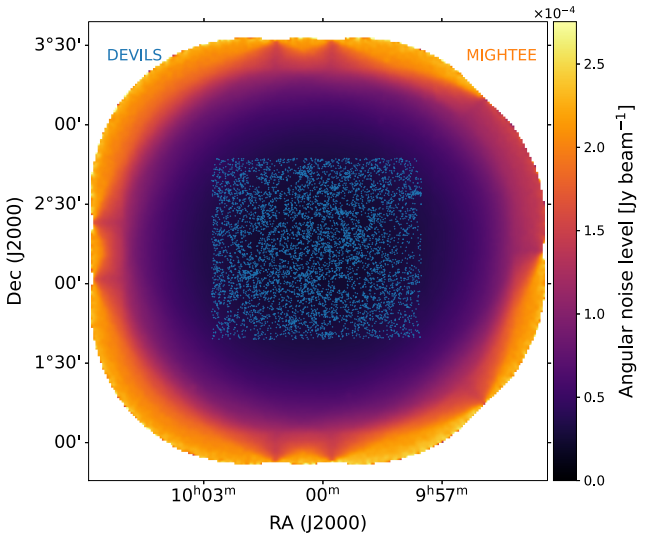

Figure 1. DEVILS spectroscopic samples overlaid on the MIGHTEE field. The colour scheme indicates the noise level of MIGHTEE DR1 L1 spectral data on a projected two-dimensional sky.

Table 1. Key parameters of the MIGHTEE DR1 L1 spectral data.

Survey area	4.94–6.49 deg^2
Integration time	94.2 h
Frequency range	960–1150 MHz
Channel width	104.5 kHz
Synthesized beam	14.8 arcsec, 19.6 arcsec ($r = 0, 0.5$)
Sensitivity (Median 1σ RMS)	40 μJy beam^{-1} ($r = 0.5$)

covering approximately ∼6 deg^2 for *L1* band. Each pointing was imaged using robustness parameters of 0.0 and 0.5 after two rounds of Radio Frequency Interference (RFI) flagging, self-calibration, and visibility-domain continuum subtraction. Subsequently, all pointings were combined for homogenization, mosaicking and an additional image-domain continuum subtraction (I. Heywood et al. 2024). We show the averaged noise level of the *L1* data across the sub-band in Fig. 1, where the galaxies with optical spectroscopy sit in the deepest region of our survey field. We list a few key parameters of the MIGHTEE DR1 L1 spectral data in Table 1 which are used in this paper.

2.2 Ancillary data

The MIGHTEE COSMOS field is covered by multiwavelength photometric and spectroscopic surveys ranging from X-ray to far-infrared bands (e.g. J.-C. J. Cuillandre et al. 2012; H. J. McCracken et al. 2012; H. Aihara et al. 2018, 2019; L. J. M. Davies et al. 2018). We use the Deep Extragalactic VIsible Legacy Survey (DEVILS; L. J. M. Davies et al. 2018) for stellar properties, which are constructed in A. Hashemizadeh et al. (2022). DEVILS is a magnitude-limited spectroscopic and multiwavelength survey, with the spectroscopic observations taken with the Anglo-Australian Telescope, providing spectroscopic redshift completeness of >95 per cent to Y-mag <21.2 mag. This spectroscopic sample has derived physical properties, such as colour, stellar mass, and star formation rate based on fitting the full spectral energy distribution with the modelling

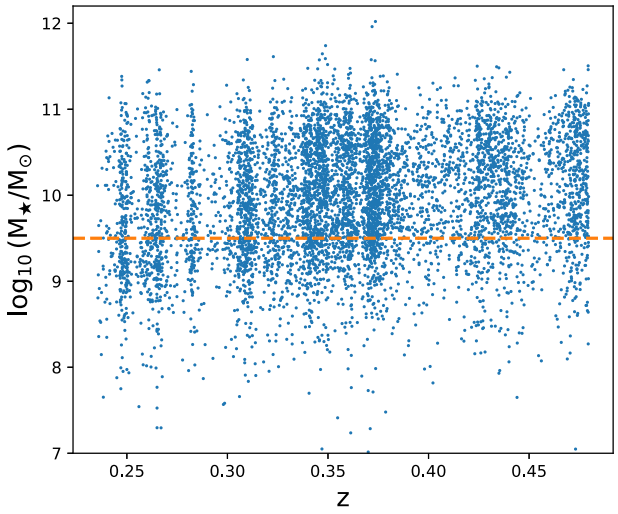

Figure 2. Stellar mass as a function of redshift. The dashed line is the limit of the sample completeness of $\log_{10}(M_\star/\mathrm{M}_\odot) = 9.5$.

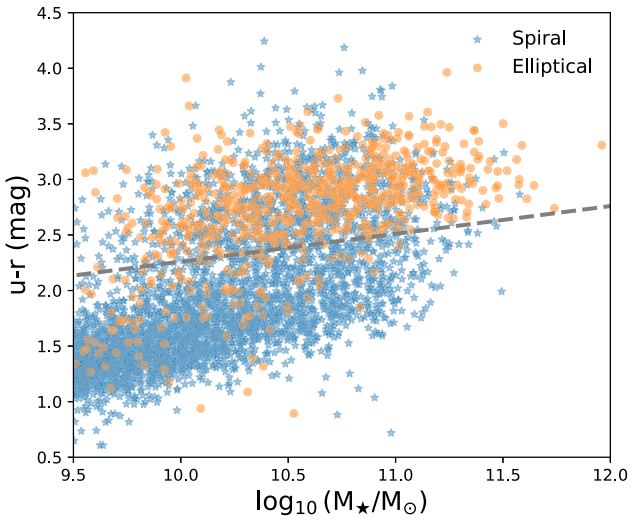

Figure 3. Colour (u-r) against the stellar mass. The blue stars are spirals while the orange dots are ellipticals. The dashed line is from K. Schawinski et al. (2014) for seperating the full sample into blue and red subsamples.

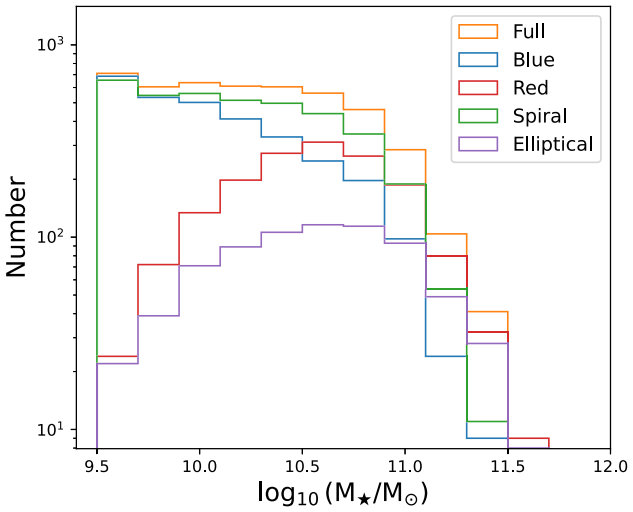

Figure 4. Histogram of the stellar mass for all galaxy samples. The orange, blue, red, green, and purple are the full sample, blue, red, spiral, and elliptical subsamples.

code PROSPECT which has well-motivated parametrizations for dust attenuation, star formation histories, and metallicity evolution (J. E. Thorne et al. 2021). In this paper, we limit the stellar mass to $\log_{10}(M_\star/\mathrm{M}_\odot) \geq 9.5$ to reduce the effects of incompleteness (see Fig. 2) and to include the morphological classifications following the same practice in A. Hashemizadeh et al. (2022).

2.3 Morphology and colour

The optical morphologies of the catalogued galaxies are classified into pure disc (D), pesudo/diffuse bulge + disc (pBD), classical bulge + disc (cBD), elliptical (E), compact (C), and hard (H). We group the D, pBP, and cBD as 'Spirals (or disc galaxies)', and also combine the C and E as 'Ellipticals (or Spheroids)' since the C subcategory is dominated by unresolved and most likely compact spheroidal systems (A. Hashemizadeh et al. 2022). The sample for visual inspection is selected to have large enough surface brightness and angular size, to be visually classified in the COSMOS *Hubble Space Telescope* data, based on a number of quality checks outlined in A. Hashemizadeh et al. (2021). The process of morphological classification initially used a number of automatic pre-classification methods followed by a full visual inspection by multiple classifiers. If the checker felt that the source was erroneously classified it was removed. All erroneous sources were then reclassified by each classifier independently. The final morphology classification is taken where the majority of classifiers agree. This process is described in more detail in A. Hashemizadeh et al. (2021).

The galaxies are also well separated into blue and red colours (u-r) in Fig. 3 using the upper limit of green valley galaxies in K. Schawinski et al. (2014). The u-band images for COSMOS field were obtained as part of the Canada-France-Hawaii Telescope Legacy Survey (CFHT-LS1),[1] supplemented by independent CFHT observations outlined in P. Capak et al. (2007), and the r-band images in this region were from the new second public data release (H. Aihara et al. 2019) of the Subaru Telescope's Hyper Suprime-Cam Subaru Strategic Program (H. Aihara et al. 2018). The Planck $E(B-V)$ map was used to correct the measured magnitudes for Galactic extinction, and the attenuation correction for each band was determined in the traditional manner (i.e. $A_x = [A_x/E(B-V)] \times E(B-V)$) by using the extinction coefficients listed in table 2 of L. J. M. Davies et al. (2021). Overall, the blue and red galaxies correlate with the spirals and ellipticals, respectively. However, we note that a large fraction of red spirals (i.e. blue stars in the upper panel of Fig. 3) exist, indicating a significantly reduced star formation rate in these galaxies compared to typical blue spirals, often caused by a depletion of gas needed for new stars to form, potentially due to environmental factors, such as ram pressure stripping in galaxy clusters or internal processes such as strong stellar feedback.

We show the histograms of the full galaxy sample, and the subsamples based on the morphology and colour classifications in Fig. 4. Clearly, the blue or spiral galaxies trace the majority of the full sample and their numbers drop as the stellar mass increases. The

[1] http://www.cfht.hawaii.edu/Science/CFHLS

spirals have even larger counts at the massive end compared to the blue galaxies as a fair fraction of red spirals exist (e.g. K. L. Masters et al. 2010; S. Mahajan et al. 2019), although a different colour (e.g. *NUV-r*) selection may reduce the fraction of red spirals to a certain degree (S. Zhou et al. 2021). In contrast, the red or elliptical galaxies are concentrated in the intermediate mass range, and we can see that the number of red spirals is on the same order of magnitude as that of the red ellipticals. Overall, the red galaxies and ellipticals constitute only a small fraction of the total galaxy population, except for the high-mass end of $\log_{10}(M_\star/{\rm M}_\odot) > 10.5$.

2.4 Flux extraction

The H I fluxes were measured from the MIGHTEE L1 spectral cube based on the angular positions and spectroscopic redshifts of objects in the ancillary galaxy catalogue. We first extracted cubelets centred on all catalogued sources with an angular aperture size of 16 arcsec and a spectral window of 1500 km s^{-1}. We further restrict the spectral window to 600 km s^{-1} at the centre of the full spectra for measuring the flux density of the H I line to minimize the level of source confusion (H. Pan et al. 2020), while balancing the need to include all flux without significantly increasing the noise given that the maximum H I line width is ∼500 km s^{-1} (A. A. Ponomareva et al. 2021). The rest of the spectral windows serve as a measurement of the spectral baseline that is subsequently removed from the central spectra. We then measure the integrated flux, $S_{\rm m}$, from the extracted flux densities, while correcting for the total beam area. The total area under a 2D Gaussian is exactly twice the area integrated within its full width at half-maximum ellipse. The correcting factor for our extraction window is slightly lower than the typical beam size (∼20 arcsec) at the frequency range of 960–1150 MHz. Therefore, we correct the integral flux numerically based on the integral to peak flux for a bright maser discovered by M. J. Jarvis et al. (2024) in Appendix A. The minor evolution of the beam size within this frequency range is also taken into account (I. Heywood et al. 2024). We quantify the flux uncertainties by moving the flux extraction box to 100 random positions surrounding the source in a distance range of 5–10 beams and computing their standard deviation. We do not require a formal H I detection in order to measure the flux since we extract the H I flux based on the source location from an optical catalogue. We also note that we are extracting fluxes below the nominal noise threshold of the data, as such the fluxes that we are measuring are not cleaned, but are beam-corrected fluxes from the synthesized beam. However, the side lobes within the MIGHTEE H I sythesized beam are very low level for the robust = 0.5 spectral cube we use in this paper,[2] as such we do not expect significant offsets in the measured flux densities. We also carry out the same experiment with the robust = 0.0 cube and find consistent results for all our analyses, from which we can infer that the flux extraction is robust.

We show the distribution of the signal-to-noise ratio ($\frac{S_{\rm m}}{\sigma_{\rm n}}$) of the measured flux in solid lines in Fig. 5. Although there are some luminous H I sources present in our full sample, the majority of the extracted fluxes are below the $5\sigma_{\rm n}$ detection threshold. As expected, the blue (or spiral) galaxies dominate the high-signal-to-noise ratio (SNR) end since they represent the most H I-rich population of galaxies. We also show the histogram of the measured noise with the dashed orange line for the full sample at offset from the spectroscopic

[2]In Fig. A3, we show the ratio of the integrated to peak flux of the unresolved OH Megamaser from M. J. Jarvis et al. (2024), which shows that the flux extracted at 16 arcsec is consistent with the synthesized beam.

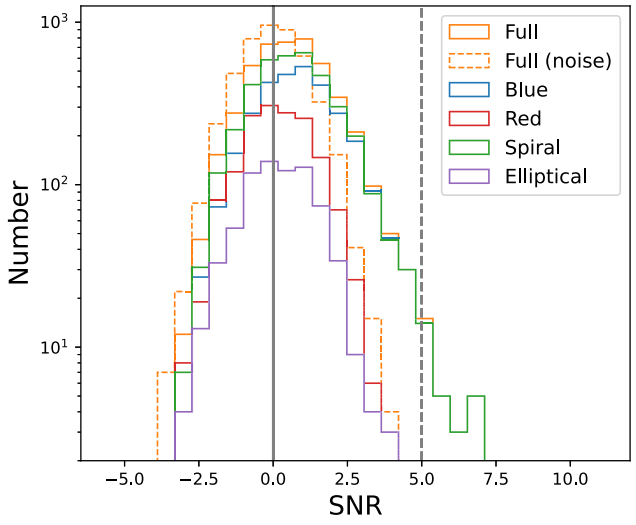

Figure 5. Distribution of SNR of the measured flux for all galaxy samples. The orange, blue, red, green, and purple are the full sample, blue, red, spiral, and elliptical subsamples. The dashed grey line indicates a nominal detection threshold of 5σ. The dashed line is for the measured noise at positions offset from the optical galaxy locations.

source position by five times the beam size, demonstrating quasi-Gaussian noise behaviour in comparison to the obvious 'long tail' feature for the full galaxy sample due to the H I signal at the source location. We are essentially modelling the difference between the distribution of measurements from the offset position and that of the measurement at the position of the galaxies, with each measurement weighted by its noise. The weighting scheme is similar to the approach employed in traditional stacking investigations (e.g. J. Healy et al. 2019; F. Sinigaglia et al. 2022; A. Bianchetti et al. 2025).

At the redshift range of $0.25 < z < 0.5$, a large number of our measurements are below the nominal detection threshold, therefore we only use the measured fluxes to constrain the underlying H I mass distribution rather than to calculate the individual H I masses. However, we do need to establish a relationship between the H I mass and the intrinsic flux to model the underlying H I mass distribution (see the next section for details). Under the optically thin gas assumption, we convert the intrinsic flux to an H I mass (or vice versa) via

$$M_{\rm H\,I} = 2.356 \times 10^5 D_{\rm L}^2 (1+z)^{-1} S, \quad (1)$$

where $M_{\rm H\,I}$ is the H I mass in solar masses, $D_{\rm L}$ is the luminosity distance in Mpc, and S is the integrated flux in Jy km s^{-1} (M. Meyer et al. 2017).

3 BAYESIAN ANALYSIS

3.1 Bayesian framework

Our analysis is based on Bayes' theorem:

$$\mathcal{P}(\Theta|D,H) = \frac{\mathcal{L}(D|\Theta,H)\Pi(\Theta|H)}{\mathcal{Z}(D|H)}, \quad (2)$$

where $\mathcal{P}$ represents the posterior distribution of the model parameters Θ, given the data D and a model H. The likelihood $\mathcal{L}$ quantifies the probability of the data D given the parameters and the model. The prior Π reflects our initial knowledge or assumptions about the

parameter values. The Bayesian evidence $\mathcal{Z}$ acts as a normalization factor and is expressed as an integral over the n-dimensional parameter space Θ:

$$\mathcal{Z}(D|H) = \int \mathcal{L}(D|\Theta, H)\Pi(\Theta|H)\mathrm{d}^n\Theta. \tag{3}$$

The evidence $\mathcal{Z}$ is essential for model selection, as it represents the probability of the data given a model, marginalized over all free parameters. By comparing evidences, we can quantitatively evaluate the relative performance of different models. The difference in the logarithm of the evidences, $\Delta\ln(\mathcal{Z}) = \ln(\mathcal{Z}_\mathcal{B}) - \ln(\mathcal{Z}_\mathcal{A})$, is known as the Bayes factor and indicates how much better Model B is compared to Model A. This method naturally penalizes overly complex models by accounting for their flexibility.

We adopt the criteria from H. Pan et al. (2023), where $\Delta\ln(\mathcal{Z}) < 1$ is categorized as 'not significant,' $1 < \Delta\ln(\mathcal{Z}) < 2.5$ as 'significant,' $2.5 < \Delta\ln(\mathcal{Z}) < 5$ as 'strong,' and $\Delta\ln(\mathcal{Z}) > 5$ as 'decisive.' For our analysis, we use MULTINEST (F. Feroz, M. P. Hobson & M. Bridges 2009; J. Buchner et al. 2014), an efficient and robust Bayesian inference tool commonly applied in cosmology and particle physics. MULTINEST allows us to sample the parameter space, explore the posterior distribution for parameter estimation, and calculate the Bayesian evidence for model comparison.

3.2 Likelihood

The relationship between the H I mass and stellar mass of galaxies can be fully described by a bivariate distribution function of H I mass and stellar mass, i.e. the conditional H I mass function on the stellar mass.

We first assume the probability of having a H I mass ($M_{\rm H\,I}$) at a given stellar mass ($M_\star$) follows the normal function,

$$P(M_{\rm H\,I}|M_\star) = \frac{1}{\sqrt{2\pi}\sigma_{\rm H\,I}} e^{-\frac{1}{2}\left(\frac{\log_{10}(M_{\rm H\,I})-\mu}{\sigma_{\rm H\,I}}\right)^2}, \tag{4}$$

where $\mu = a[\log_{10}(M_\star) - 10] + b$, and $\sigma_{\rm H\,I}$ is the intrinsic scatter in H I mass at a given stellar mass. We define this normal function as our base '**Model A**'.

A priori we do not know the underlying relation between stellar mass and H I mass. We therefore also define two additional models where the underlying distribution of H I mass is allowed to be asymmetric.

The first asymmetric model is a conditional probability density with the form of a Schechter function:

$$P(M_{\rm H\,I}|M_\star) = \ln(10)\phi_*\left(\frac{M_{\rm H\,I}}{M_*}\right)^{\alpha+1} e^{-\frac{M_{\rm H\,I}}{M_*}}, \tag{5}$$

where $\log_{10}(M_*) = a[\log_{10}(M_\star) - 10] + b$ and α correspond to the characteristic mass and faint-end slope respectively, and ϕ_* is the normalization such that the integration of equation (5) over the logarithmic H I mass is equal to 1, therefore not a free parameter. We note this Schechter function form as '**Model B**'.

The second asymmetric model that we propose is a skew-normal probability density distribution given by:

$$P(M_{\rm H\,I}|M_\star) = \frac{2}{\sigma\sqrt{2\pi}} e^{-\frac{(\log_{10}(M_{\rm H\,I})-\mu)^2}{2\sigma^2}} \Phi\left(\alpha\cdot\frac{\log_{10}(M_{\rm H\,I})-\mu}{\sigma}\right), \tag{6}$$

where $\alpha, \sigma, \mu = a[\log_{10}(M_\star) - 10] + b$ are free parameters, and $\Phi(x) = \frac{1}{2}\left[1 + \mathrm{erf}\left(\frac{x}{\sqrt{2}}\right)\right]$. We note this skew-normal form as '**Model C**'.

With an assumed conditional probability distribution, the probability of measuring a flux, $S_{\rm m}$, for a single source, can be expressed as

$$P(S_{\rm m}|M_\star) = \int \mathrm{d}M_{\rm H\,I} P(M_{\rm H\,I}|M_\star) P_{\rm n}(S_{\rm m} - S(M_{\rm H\,I})), \tag{7}$$

where $S(M_{\rm H\,I})$ is given by equation (1), and $P_{\rm n}$ is the noise distribution which we assume to be consistent with a normal distribution centered on zero with standard deviation $\sigma_{\rm n}$. Fig. B2 in I. Heywood et al. (2024) shows that the mean Pearson kurtosis are close to the ideal Gaussian value of 3, and a slight deviation from Gaussianity for the noise behaviour does not affect our main results (We tested this using a model distribution for the $M_\star - M_{\rm H\,I}$ relation and injected the simulated sources in the real data cube and performed the same analaysis. Full details can be found in Appendix B). We emphasize that this assumption is the same for the more traditional stacking technique, where the signal is weighted by the noise measured in nearby offset positions or either side of the emission line, also under the assumption of Gaussian noise (e.g. J. Healy et al. 2019).

The likelihood of all the sources having the measured fluxes, given the model and known stellar masses, is given by

$$\begin{aligned}\mathcal{L} \propto \prod_{\rm source} & P(S_{\rm m}|M_\star, \mathrm{A}(a, b, \sigma_{\rm H\,I}),\\ & \text{or } |M_\star, \mathrm{B}(a, b, \alpha),\\ & \text{or } |M_\star, \mathrm{C}(a, b, \alpha, \sigma)).\end{aligned} \tag{8}$$

By maximizing equation (8), we obtain the best-fitting $M_{\rm H\,I} - M_\star$ relation described by Models A, B, and C for a given galaxy sample.

At this point, we would like to note again that our equation (7) does not require a formal H I detection to calculate the probability of measuring the flux, $S_{\rm m}$, since this flux can always be extracted based on the source location from an optical catalogue regardless of its SNR in the radio image. The $\sigma_{\rm n}$ is measured on a per source basis from propagating the per channel noise measurement over the 600 km s^{-1} spectral window and $\sigma_{\rm n}$ is not assumed to be constant. A higher noise level for a low-SNR source will result in a wider $P_{\rm n}$, which will reduce the contribution of the $S_{\rm m}$ for this source to the total likelihood of the equation (8) for constraining the assumed model of $P(M_{\rm H\,I}|M_\star)$ in the equations (4)–(6).

The average of logarithmic H I mass for a conditional distribution of $\log_{10}(M_{\rm H\,I})$ on the stellar mass is

$$\langle\log_{10}(M_{\rm H\,I})\rangle = \int \log_{10}(M_{\rm H\,I}) P(M_{\rm H\,I}|M_\star)\mathrm{d}\log_{10}(M_{\rm H\,I}). \tag{9}$$

In comparison, the logarithmic of average H I mass is given from our modelling by

$$\log_{10}(\langle M_{\rm H\,I}\rangle) = \log_{10}\left(\int M_{\rm H\,I} P(M_{\rm H\,I}|M_\star)\mathrm{d}\log_{10}(M_{\rm H\,I})\right). \tag{10}$$

We note that the $\log_{10}(\langle M_{\rm H\,I}\rangle)$ could also be measured directly from the standard co-adding stacking approach, i.e. $\log_{10}\left(\frac{\sum w M^{\rm m}_{\rm H\,I}}{\sum w}\right)$, where w is the weight of each galaxy taken as the reciprocal of the noise variance, and $M^{\rm m}_{\rm H\,I}$ is the measured H I mass which is the intrinsic $M_{\rm H\,I}$ added to the noise. To differentiate these two measurements, we denote the latter one as 'Co-adding' measurement.

The conditional H I mass function or bivariate distribution can then be written as

$$\Phi(M_{\rm H\,I}|M_\star) = P(M_{\rm H\,I}|M_\star)\Phi(M_\star), \tag{11}$$

Table 2. Parameters and priors for three Models used to measure the H I and stellar mass relation of the Full, Blue, and Spiral subsamples.

Model	Parameter	Prior probability distribution
A	a	uniform $\in [-2.5, 2.5]$
	b	uniform $\in [7, 12]$
	$\sigma_{\rm HI}$	uniform $\in [0, 2]$
B	a	uniform $\in [-2.5, 2.5]$
	b	uniform $\in [7, 12]$
	α	uniform $\in [-2.5, 2.5]$
C	a	uniform $\in [-2.5, 2.5]$
	b	uniform $\in [8, 13]$
	α	uniform $\in [-47.5, 2.5]$
	σ	uniform $\in [0, 3]$

where $\Phi(M_\star)$ is the galaxy stellar mass function (GSMF). Therefore, the marginalization of $\Phi(M_{\rm HI}|M_\star)$ over $M_\star$ results in the H I mass function. In this paper, we present the H I mass function for a stellar mass-selected sample with $\log_{10}(M_\star/{\rm M}_\odot) > 9.5$ as

$$\begin{aligned}\Phi(M_{\rm HI})_{9.5} &= \int_{9.5}^{+\infty} \Phi(M_{\rm HI}|M_\star){\rm d}\log_{10}(M_\star) \\ &= \int_{9.5}^{+\infty} P(M_{\rm HI}|M_\star)\Phi(M_\star){\rm d}\log_{10}(M_\star).\end{aligned} \tag{12}$$

We use the GSMF measurements for the full sample, spirals, and ellipticals from A. Hashemizadeh et al. (2022), and also split the GSMF of the full sample into GSMFs for the blue and red galaxies.

3.3 Priors

The priors, which encode our knowledge of each parameter before incorporating new experimental data, are listed in Table 2 for the Full, Blue, and Spiral subsamples. Minor adjustments are made for the red and elliptical subsamples due to their small sample sizes.

4 RESULTS

4.1 The $M_{\rm HI} - M_\star$ relation for the full sample

We present the best-fitting bivariate distribution of H I mass and stellar mass for the full sample in Fig. 6 (top row), with the three best-fitting models of Normal, Schechter, and Skew normal from the left to right panels, respectively (the measured bivariate distribution is shown in Appendix A for completeness). Compared to the Normal model where the H I scatter is symmetric at a given stellar mass, the Schechter and Skew normal models have the capability of capturing asymmetry in the underlying H I mass distribution as a function of the stellar mass. The posterior probability distributions for all parameters in the three models are well converged as shown in the

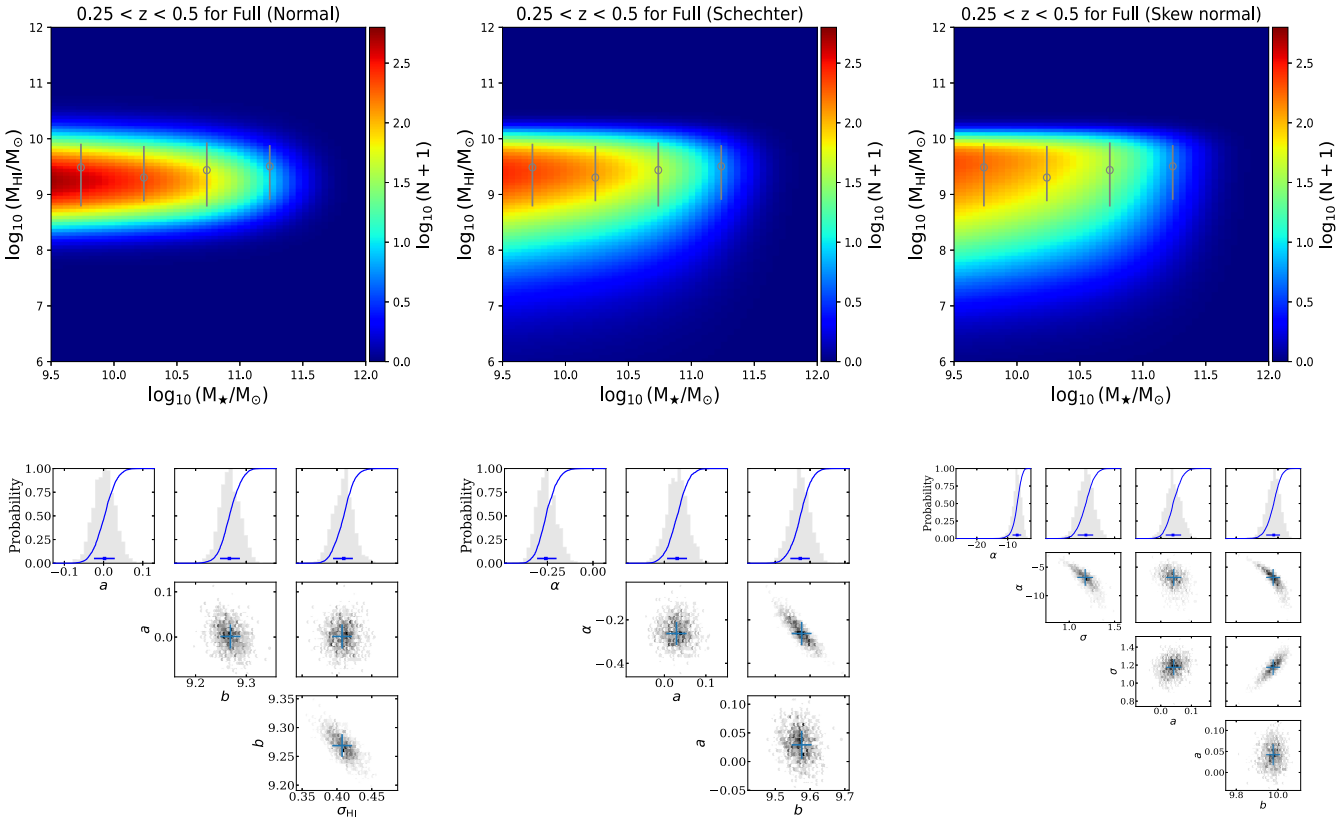

Figure 6. Top row: bivariate distribution of H I mass and stellar mass for the full sample at $0.25 < z < 0.5$. Three models (Normal, Schechter, Skew normal) are fit to the data from left to right panels. The grey dots with the error bars correspond to the 16th, 50th, and 84th percentiles for the H I mass in four stellar mass bins from the SIMBA simulation (R. Davé et al. 2019). Bottom row: posterior probability distributions for the three fitting models correspondingly from from left to right panels. The grey histograms represent the marginal posterior probabilities (1 or 2 dimensional), while the blue curves indicate the cumulative distributions. In the two-dimensional (2D) posterior plots, the blue crosses mark the parameter set with the maximum likelihood, and the 1σ error bars are estimated from the 1D marginal posterior distributions.

bottom row, and our data decisively favour the asymmetric H I mass distribution for the full galaxy sample, given that the Bayes factors of the Schechter (Model B) and Skew normal (Model C) models compared to the normal distribution (Model A) are much larger than the critical threshold for most stellar mass bins as reported in Table 3. The Skew normal has no better performance than the Schechter model, despite the fact that the Skew normal has four free parameters which add a certain level of flexibility of fitting for the data in comparison with the Schechter form. The physics behind this stems from the fact that the H I gas mass fraction is non-linear with stellar mass and although there appears to be a strong upper envelope in H I mass as a function of stellar mass (e.g. H. Pan et al. 2023), the distribution of H I mass is not likely to have such a strong low-H I mass envelope and that this is likely to be different for spheroids and disc galaxies. We also show the band of H I mass for the 16th, 50th, and 84th percentiles in four stellar mass bins at $0.25 < z < 0.5$ from the SIMBA simulation (R. Davé et al. 2019). Overall, the bivariate distribution of the H I mass and stellar mass traces the SIMBA percentiles, especially for the Schechter and Skew normal models where the high-density area just above the mass limit is more consistent between our model and the simulated galaxies.

4.2 Log of the average versus average of the log

The average of the logarithmic H I mass, i.e. $\langle \log_{10}(M_{\rm H\,I}) \rangle$, and the logarithmic average of the H I mass, i.e. $\log_{10}(\langle M_{\rm H\,I} \rangle)$, as a function of the stellar mass, are shown in solid and dashed lines, respectively, for the full sample in Fig. 7. The three models of Normal, Schechter, and Skew normal are colour-coded in blue, orange, and green. The difference between $\langle \log_{10}(M_{\rm H\,I}) \rangle$ and $\log_{10}(\langle M_{\rm H\,I} \rangle)$ for all models is considerable with 0.2–0.3 dex for Normal and Schechter models, and ∼0.5 dex for the Skew normal. The solid dots are the logarithmic of direct averaging the measured $M_{\rm H\,I}$, labelled as 'Co-adding' to be differentiated from the $\log_{10}(\langle M_{\rm H\,I} \rangle)$ driven from our Bayesian modelling. The $\log_{10}(\langle M_{\rm H\,I} \rangle)$ would be equal to the Co-adding measurement if our models could perfectly describe the conditional H I mass distribution on the stellar mass. As shown, the dashed lines are indeed in excellent agreement with the solid dots overall, except for the most massive end of $\log_{10}(M_\star/{\rm M}_\odot) > 11$ where the number of sources is only on a scale of a few hundreds, hence contributing low-number statistical uncertainties to our modelling. The overall minimal offsets (less than 0.1 dex) indicate that the modelling of the H I distribution is not in perfect agreement with the bivariate distribution of H I mass and stellar mass from traditional stacking. This may be because the relationship is more complex and is not fully captured by our simple analytic models with three or four parameters. On the other hand, the traditional stacking method is sensitive to outliers, which could result in a biased estimate of the average H I mass, whereas our modelling of the underlying distribution provides more information on this.

On the other hand, the $\langle \log_{10}(M_{\rm H\,I}) \rangle$ for our base Model A (i.e. the Normal model) also broadly agrees with that from H. Pan et al. (2023) where their average of the logarithmic H I mass is derived from the H I detections at $z < 0.08$. Such an agreement could indicate minimal evolution on the H I distribution in massive galaxies at $z < 0.5$. However, the $\langle \log_{10}(M_{\rm H\,I}) \rangle$ is notably lower than the measurement from H. Pan et al. (2023) at $\log_{10}(M_\star/{\rm M}_\odot) < 10.5$ but slightly higher than that at $\log_{10}(M_\star/{\rm M}_\odot) > 11$. We return to this when discussing the conditional H I mass function in Section 4.5.

The finding is also in accord with F. Sinigaglia et al. (2022), suggesting a scenario where the massive galaxies have undergone a significant H I replenishment through some accretion mechanism, such as minor mergers or gas accretion from the nearby cosmic web (D. Kleiner et al. 2017), to maintain their neutral gas storage during the last ∼4 Gyr. However, we note that the approach taken here using a large number of non-H I detections is quite different from H. Pan et al. (2023) using a limited number of H I detections with large statistical uncertainties of ∼ 0.3 dex. The shallow slopes across all models suggest the existence of an upper H I mass limit beyond which a galaxy can no longer retain more H I gas, independent of the amount of their stellar component. This trend is also in line with the findings from S. Huang et al. (2012), N. Maddox et al. (2015), and H. Pan et al. (2023) on the non-linear $M_{\rm H\,I} - M_\star$ scaling relation with a transition stellar mass between 10^9 and $10^{9.5}{\rm M}_\odot$.

4.3 Colour dependence

The blue galaxies are generally H I gas rich compared to the red population; therefore, they should occupy a different parameter space of H I mass and stellar mass from red galaxies. We now investigate the colour dependence of the $M_{\rm H\,I} - M_\star$ relation by dividing the full sample into blue and red galaxies as illustrated in Fig. 3.

In Fig. 8, we show the bivariate distribution of H I mass and stellar mass for the blue and red samples in the left and right panels, with the three best-fitting models from top to bottom panels. Indeed, the blue galaxies are tightly clustered in the lowest stellar mass bins of $9.5 < \log_{10}(M_\star/{\rm M}_\odot) < 10.5$, and relatively high H I mass range of $9 < \log_{10}(M_{\rm H\,I}/{\rm M}_\odot) < 10$, especially with the preferred models of Schechter and Skew normal. The red galaxies instead sit broadly in the intermediate stellar mass range of $9.5 < \log_{10}(M_\star/{\rm M}_\odot) < 11.5$, and the H I mass range of $7.5 < \log_{10}(M_{\rm H\,I}/{\rm M}_\odot) < 9.5$, therefore tend to have lower average H I mass than the blue galaxies. This trend can be noted more clearly in the left panel of Fig. 9, where the $\langle \log_{10}(M_{\rm H\,I}) \rangle$ and $\log_{10}(\langle M_{\rm H\,I} \rangle)$ of red galaxies in red solid and dashed lines are both lower than those of the full sample. The difference between the $\log_{10}(\langle M_{\rm H\,I} \rangle)$ derived from our modelling and dots measured from the 'Co-adding' experiment is due to the small sample size of red galaxies for their broad distribution in the $M_{\rm H\,I} - M_\star$ space.

The $\log_{10}(\langle M_{\rm H\,I} \rangle)$ of the blue galaxies (blue dashed line) is in good agreement with the stacking result (grey dashed line) from F. Sinigaglia et al. (2022) where they use the MIGHTEE E.S. data to measure the logarithmic average of the H I mass as a function of the stellar mass bin for selected star-forming galaxies, with a minor differing slope. We note that A. Bianchetti et al. (2025) use both MIGHTEE E.S. and COSMOS H I Large Extra-galactic Survey (X. Fernández et al. 2016) data and measure a relatively steeper slope than that from F. Sinigaglia et al. (2022) mostly due to the difference in the spectroscopic catalogue used.

In the right panel of Fig. 9, we show the difference for our three best-fitting models to the blue galaxy sample. Although the logarithmic average of the H I mass, $\log_{10}(\langle M_{\rm H\,I} \rangle)$, among the three models (dashed lines) is in excellent agreement, the average of the logarithmic H I mass, $\langle \log_{10}(M_{\rm H\,I}) \rangle$, demonstrates notable differences. This is fundamentally rooted in their different mathematical forms, where the logarithmic average is only sensitive to the the massive end of $\log_{10}(M_{\rm H\,I})$ distribution while the average of the logarithmic is sensitive to the whole mass space of $\log_{10}(M_{\rm H\,I})$ distribution. Therefore, the difference of these models manifests in the $\langle \log_{10}(M_{\rm H\,I}) \rangle$ generally. Greater asymmetry in the fitting model results in a larger deviation of $\langle \log_{10}(M_{\rm H\,I}) \rangle$ from the value predicted by our symmetrical Model A.

The maximum difference on the zero point of the $\langle \log_{10}(M_{\rm H\,I}) \rangle$ as a function of the stellar mass between Models A, B, and C is about

Table 3. Best-fitting parameters of the measured conditional H I mass distribution with Models A, B, and C (corresponding to Normal, Schechter, and Skew normal models, respectively) for the full galaxy sample, blue, red, spiral, and elliptical subsamples at $0.25 < z < 0.5$. Fits are omitted for subsamples with sizes too small to produce robust results.

Sample	Model	Parameter	$9.5 < \log_{10}(M_\star) < 10$	$10 < \log_{10}(M_\star) < 10.5$	$10.5 < \log_{10}(M_\star) < 11$	$11 < \log_{10}(M_\star) < 11.5$	$9.5 < \log_{10}(M_\star)$
		a	0.05 ± 0.13	-0.17 ± 0.15	0.46 ± 0.19	-0.48 ± 0.65	-0.0 ± 0.03
	A	b	9.29 ± 0.04	9.28 ± 0.04	8.88 ± 0.15	9.55 ± 0.74	9.23 ± 0.02
		$\sigma_{\rm H\,I}$	0.36 ± 0.02	0.39 ± 0.02	0.44 ± 0.03	0.56 ± 0.09	0.41 ± 0.01
		a	0.06 ± 0.13	-0.07 ± 0.14	0.49 ± 0.17	-0.47 ± 0.59	0.03 ± 0.03
	B	b	9.44 ± 0.06	9.53 ± 0.06	9.26 ± 0.14	10.37 ± 0.7	9.53 ± 0.03
		α	0.0 ± 0.13	-0.21 ± 0.11	-0.37 ± 0.09	-0.69 ± 0.12	-0.25 ± 0.06
Full		$\Delta \ln(\mathcal{Z})$	6.28 ± 0.09	5.62 ± 0.03	9.26 ± 0.17	1.47 ± 0.22	19.89 ± 0.45
		a	0.06 ± 0.12	-0.04 ± 0.13	0.51 ± 0.14	-0.41 ± 0.53	0.04 ± 0.02
		b	9.91 ± 0.06	9.94 ± 0.06	9.68 ± 0.12	10.38 ± 0.69	9.94 ± 0.03
	C	α	-5.74 ± 9.27	-6.46 ± 3.48	-11.48 ± 10.11	-4.78 ± 4.7	-6.8 ± 1.44
		σ	0.97 ± 0.13	1.11 ± 0.14	1.42 ± 0.12	1.45 ± 0.36	1.17 ± 0.09
		$\Delta \ln(\mathcal{Z})$	5.23 ± 0.09	4.77 ± 0.11	11.85 ± 0.34	-0.21 ± 0.19	19.03 ± 0.09
		a	0.23 ± 0.14	0.09 ± 0.13	0.7 ± 0.18	-0.11 ± 0.63	0.22 ± 0.03
	A	b	9.4 ± 0.04	9.44 ± 0.04	9.06 ± 0.14	9.76 ± 0.72	9.4 ± 0.02
		$\sigma_{\rm H\,I}$	0.33 ± 0.02	0.31 ± 0.02	0.32 ± 0.03	0.34 ± 0.09	0.32 ± 0.01
		a	0.21 ± 0.12	0.14 ± 0.13	0.71 ± 0.18	-0.3 ± 0.56	0.22 ± 0.03
	B	b	9.43 ± 0.06	9.35 ± 0.07	9.0 ± 0.15	10.04 ± 0.65	9.39 ± 0.03
		α	0.23 ± 0.17	0.52 ± 0.21	0.43 ± 0.25	0.18 ± 0.49	0.35 ± 0.11
Blue		$\Delta \ln(\mathcal{Z})$	4.23 ± 0.05	5.71 ± 0.43	7.16 ± 0.28	1.2 ± 0.05	13.58 ± 0.03
		a	0.2 ± 0.12	0.17 ± 0.12	0.6 ± 0.16	-0.49 ± 0.63	0.21 ± 0.02
		b	9.91 ± 0.07	9.93 ± 0.06	9.69 ± 0.12	10.76 ± 0.74	9.94 ± 0.03
	C	α	-4.26 ± 9.79	-5.61 ± 3.92	-10.69 ± 13.98	-5.34 ± 15.67	-5.69 ± 1.77
		σ	0.77 ± 0.13	0.75 ± 0.11	0.83 ± 0.09	0.88 ± 0.29	0.8 ± 0.07
		$\Delta \ln(\mathcal{Z})$	2.66 ± 0.18	3.07 ± 0.03	8.83 ± 0.06	0.67 ± 0.07	14.4 ± 0.76
		a	–	2.45 ± 2.27	-0.41 ± 0.58	-1.17 ± 0.98	0.25 ± 0.13
	A	b	–	7.46 ± 1.0	9.21 ± 0.43	10.06 ± 1.17	8.47 ± 0.15
		$\sigma_{\rm H\,I}$	–	0.62 ± 0.15	0.29 ± 0.15	0.5 ± 0.26	0.49 ± 0.08
		a	–	5.12 ± 3.36	-0.37 ± 0.55	-0.66 ± 1.04	0.24 ± 0.13
	B	b	–	7.4 ± 1.38	9.12 ± 0.47	10.25 ± 1.16	9.01 ± 0.33
		α	–	-0.84 ± 0.48	0.46 ± 0.96	-0.7 ± 1.21	-0.45 ± 0.82
Red		$\Delta \ln(\mathcal{Z})$	–	-1.0 ± 0.1	1.05 ± 0.09	0.17 ± 0.06	-0.21 ± 0.12

Table 3 – *continued*

Sample	Model	Parameter	$9.5 < \log_{10}(M_\star) < 10$	$10 < \log_{10}(M_\star) < 10.5$	$10.5 < \log_{10}(M_\star) < 11$	$11 < \log_{10}(M_\star) < 11.5$	$9.5 < \log_{10}(M_\star)$
		a	–	1.3 ± 1.29	-0.53 ± 0.57	-0.75 ± 1.24	0.22 ± 0.13
		b	–	8.58 ± 0.33	9.87 ± 0.44	9.86 ± 1.32	8.92 ± 0.17
	C	α	–	-1.82 ± 5.15	-10.52 ± 4.14	-0.91 ± 4.78	-1.38 ± 2.12
		σ	–	1.04 ± 0.38	0.92 ± 0.41	0.66 ± 0.51	0.74 ± 0.25
		$\Delta \ln(\mathcal{Z})$	–	-3.32 ± 0.1	-0.16 ± 0.11	-0.84 ± 0.06	-1.47 ± 0.11
		a	0.14 ± 0.13	-0.06 ± 0.15	0.74 ± 0.19	0.34 ± 0.68	0.1 ± 0.03
	A	b	9.34 ± 0.04	9.31 ± 0.05	8.79 ± 0.15	8.91 ± 0.81	9.29 ± 0.02
		$\sigma_{\rm H\,I}$	0.35 ± 0.02	0.38 ± 0.02	0.4 ± 0.03	0.46 ± 0.1	0.38 ± 0.01
		a	0.14 ± 0.13	0.01 ± 0.14	0.68 ± 0.17	0.23 ± 0.66	0.11 ± 0.03
	B	b	9.44 ± 0.07	9.49 ± 0.06	9.08 ± 0.14	9.47 ± 0.76	9.48 ± 0.03
		α	0.06 ± 0.15	-0.08 ± 0.12	-0.14 ± 0.13	-0.39 ± 0.23	-0.09 ± 0.07
Spiral		$\Delta \ln(\mathcal{Z})$	5.64 ± 0.36	6.07 ± 0.57	8.12 ± 0.1	0.87 ± 0.18	18.15 ± 0.03
		a	0.13 ± 0.12	0.07 ± 0.13	0.64 ± 0.15	-0.07 ± 0.61	0.11 ± 0.02
		b	9.91 ± 0.07	9.94 ± 0.06	9.62 ± 0.12	10.22 ± 0.72	9.96 ± 0.03
	C	α	-5.37 ± 8.08	-6.56 ± 4.32	-13.32 ± 12.4	-9.56 ± 14.95	-7.38 ± 2.06
		σ	0.91 ± 0.14	1.04 ± 0.15	1.23 ± 0.12	1.45 ± 0.29	1.08 ± 0.08
		$\Delta \ln(\mathcal{Z})$	4.06 ± 0.27	4.23 ± 0.09	10.7 ± 0.17	0.68 ± 0.1	19.26 ± 0.09
		a	-1.16 ± 0.91	-0.79 ± 1.16	–	–	-0.29 ± 0.18
	A	b	8.7 ± 0.4	8.92 ± 0.43	–	–	8.88 ± 0.15
		$\sigma_{\rm H\,I}$	0.41 ± 0.23	0.46 ± 0.25	–	–	0.43 ± 0.12
		a	-1.27 ± 0.79	-0.48 ± 1.08	–	–	-0.31 ± 0.17
	B	b	9.05 ± 0.39	9.23 ± 0.45	–	–	9.23 ± 0.3
		α	-0.37 ± 1.0	-0.3 ± 1.11	–	–	-0.26 ± 0.96
Elliptical		$\Delta \ln(\mathcal{Z})$	0.97 ± 0.04	0.79 ± 0.05	–	–	1.1 ± 0.07
		a	-1.23 ± 0.76	-0.01 ± 1.06	–	–	-0.32 ± 0.17
		b	9.5 ± 0.28	9.1 ± 0.37	–	–	9.64 ± 0.15
	C	α	-38.33 ± 15.43	-25.28 ± 15.78	–	–	-9.86 ± 15.99
		σ	1.38 ± 0.47	0.01 ± 0.46	–	–	1.09 ± 0.28
		$\Delta \ln(\mathcal{Z})$	0.93 ± 0.04	0.42 ± 0.05	–	–	0.6 ± 0.24

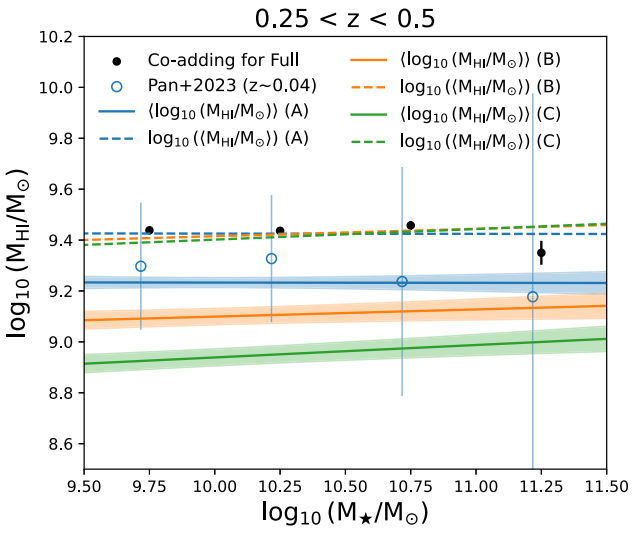

Figure 7. Best-fitting $M_{\rm HI} - M_\star$ scaling relation for the full sample. The solid and dashed lines are the $\langle \log_{10}(M_{\rm HI})\rangle$ and $\log_{10}(\langle M_{\rm HI}\rangle)$, respectively. The blue, orange, and green lines are our Model A, B, and C corresponding to the Normal, Schechter, and Skew normal distributions. The solid dots are the logarithmic of directly averaging $M_{\rm HI}$, labelled as 'Co-adding' to be differentiated from the $\log_{10}(\langle M_{\rm HI}\rangle)$ driven from our Bayesian modelling. The circles are the average of logarithmic H I mass from H. Pan et al. (2023). The shaded areas are 1σ statistical uncertainties on the $\langle \log_{10}(M_{\rm HI})\rangle$.

0.1 dex, which is smaller than that for the full sample in Fig. 7 due to a tighter $M_{\rm HI} - M_\star$ relation for the blue sample. Their slopes are rather close, and all are steep when compared to the relatively flat slopes for the full sample, indicating that the H I mass of massive blue galaxies is positively correlated with the stellar mass. This trend is also true for the red galaxies due to the existence of a large fraction of red disc galaxies. The $\langle \log_{10}(M_{\rm HI})\rangle$ for our model A (i.e. the Normal model) is slightly lower than the double-power law fitting for the underlying average H I mass for the late-type galaxies from H. Pan et al. (2023) but still within 1σ uncertainties.

The above analysis is based on the modelling of galaxies across a broad mass range of $\log_{10}(M_\star/{\rm M}_\odot) > 9.5$, with only one set of free parameters. To investigate whether we can improve the modelling by splitting the total stellar masses into individual mass bins, we plot the probability distribution of the H I mass in a typical mass bin of $10 < \log_{10}(M_\star/{\rm M}_\odot) < 10.5$ for the blue sample in Fig. 10, and show the three models of Normal, Schechter, and Skew normal from left to right panels.

The probability distributions for the broad and individual mass ranges are represented in blue and orange, respectively. The $\langle \log_{10}(M_{\rm HI})\rangle$ and $\log_{10}(\langle M_{\rm HI}\rangle)$ are shown in thin and thick dashed lines. For the blue sample, the best-fitting probability profiles from the broad mass range are in excellent agreement with those from the individual mass range for all three models, except for the regions surrounding the probability peaks. The Skew normal distribution has the largest difference between the $\langle \log_{10}(M_{\rm HI})\rangle$ and $\log_{10}(\langle M_{\rm HI}\rangle)$, as shown already in the right panel of Fig. 9. The minimal difference between the $\log_{10}(\langle M_{\rm HI}\rangle)$ and the result from the Co-adding measurement is also the same as we see at $\log_{10}(M_\star/{\rm M}_\odot) = 10.25$ in the right panel of Fig. 9. For the red galaxies, the Schechter and Skew normal models are not preferred by our data over the normal distribution, likely due to the small sample size of the red subsamples, based on the negative Bayes factor of $\Delta \ln(\mathcal{Z}) = -0.21$ for the Schechter model and the $\Delta \ln(\mathcal{Z}) = -1.47$ for the Skew normal at $\log_{10}(M_\star) > 9.5$ in Table 3.

4.4 Morphology dependence

We also split the full sample into spirals and ellipticals to study the morphology dependence of the $M_{\rm HI} - M_\star$ relation, motivated by the morphology–colour correlation of galaxies as a function of the environment (e.g. S. P. Bamford et al. 2009; P. A. A. Lopes et al. 2016). In Fig. 11, the bivariate distributions of H I mass and stellar mass for the spirals and elllipticals largely follow the features for the blue and red galaxies in Fig. 8. The Schechter and Skew normal models are favoured by our data for the spirals, with Bayes factors of $\Delta \ln(\mathcal{Z}) = 18.15 \pm 0.03$ and $\Delta \ln(\mathcal{Z}) = 19.26 \pm 0.09$, respectively. A notable difference is that the number of ellipticals is apparently lower than that of red galaxies as expected from Fig. 4. We show the SIMBA (R. Davé et al. 2019) spirals and ellipticals with the grey circles along with the error bars indicating the 16th, 50th, and 84th percentiles of the H I mass in four stellar mass bins over a similar redshift range to our MIGHTEE observations. The spirals and ellipticals in SIMBA are divided by the fraction of rotational kinetic energy ($\kappa_{\rm rot}$) = 0.7 (L. V. Sales et al. 2012; E. Elson, M. Glowacki & R. Davé 2023), according to the importance of their rotationally supported components. Overall, we find reasonably good agreement between MIGHTEE and SIMBA spirals for the bivariate distributions of H I mass and stellar mass, especially when we model the conditional H I mass distribution with the preferred Skew normal and Schechter models. However, for the ellipticals, the MIGHTEE median H I masses tend to be systematically lower than those predicted from the SIMBA simulation by ∼0.4 dex, which suggests that SIMBA may overestimate the amount of H I gas in the massive dead galaxies in line with the finding from H. Pan et al. (2023) at $z < 0.08$.

The averaged $M_{\rm HI} - M_\star$ relation for the spirals in Fig. 12 has a relatively smaller zero-point by ∼0.1 dex than for the blue galaxies, and deviates from F. Sinigaglia et al. (2022) slightly further than for the blue population which presumably is more similar to the star forming population. We note that the H I mass seems to be anticorrelated with the stellar mass for the ellipticals, indicating that more massive elliptical galaxies consume or lose their H I gas more efficiently. In contrast, the red massive galaxies include a non-negligible amount of disc galaxies which can still retain a certain fraction of H I gas across a wide stellar mass range (e.g. L. Wang et al. 2022)

4.5 Conditional H I mass function

We show the H I mass function for galaxies with $\log_{10}(M_\star/{\rm M}_\odot) > 9.5$ at $0.25 < z < 0.5$ in Fig. 13, determined using equation (12). The three best-fitting models (Normal, Schechter, Skew normal) are shown from left to right panels. We also plot the H I mass function from ALFALFA (M. G. Jones et al. 2018) for the H I galaxy population in the local Universe, without any selection based on stellar mass, along with the SIMBA H I mass function, applying the same selection criteria as imposed on our data at the same redshift. The difference between our conditional HIMF for the full sample and the ALFALFA general H I mass function (HIMF) is significant at intermediate and low H I masses, as expected as the DEVILS sample is limited to the $\log_{10}(M_\star/{\rm M}_\odot) > 9.5$ galaxies, which have the capability of hosting large amounts of H I gas (i.e. most H I gas in the local Universe resides in the high-stellar mass galaxies based on H. Pan et al. 2024 for example).

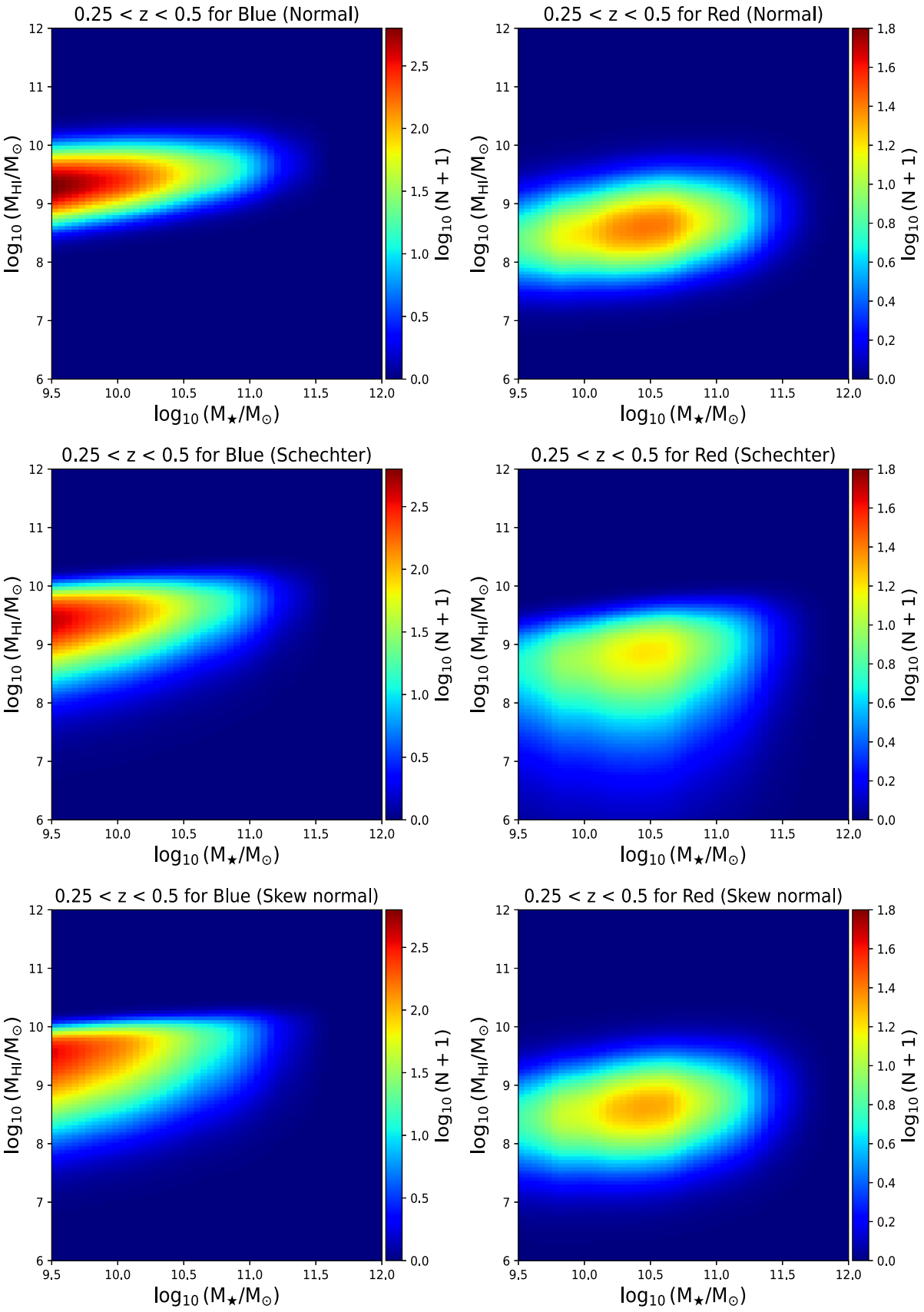

Figure 8. Bivariate distribution of H I mass and stellar mass for blue (left) and red (right) galaxies at $0.25 < z < 0.5$. Three models (Normal, Schechter, Skew normal) are fit to the data from top to bottom panels. The corresponding posteriors are appended in Fig. C1.

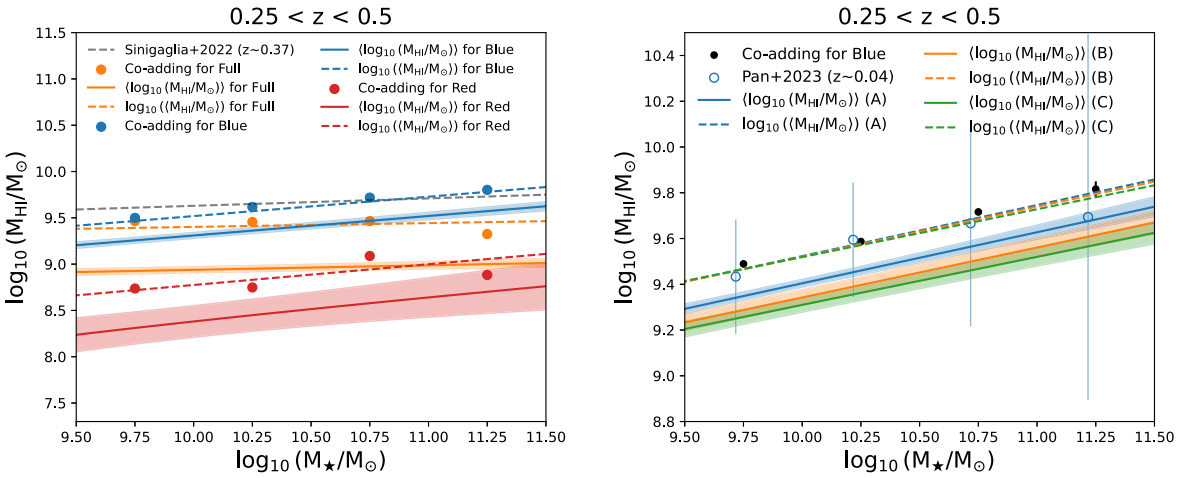

Figure 9. Left panel: best-fitting $M_{\rm HI} - M_\star$ scaling relation for the full sample, blue, and red galaxies with the Skew normal model, colour-coded by orange, blue, and red, respectively. Right panel: best-fitting $M_{\rm HI} - M_\star$ scaling relation for blue galaxies with Normal, Schechter, and Skew normal models labelled as Models A, B, and C. The solid and dashed lines are the $\langle \log_{10}(M_{\rm HI})\rangle$ and $\log_{10}(\langle M_{\rm HI}\rangle)$, respectively. The solid dots are the logarithmic of directly averaging $M_{\rm HI}$, labelled as 'Co-adding'. The dashed grey line is from F. Sinigaglia et al. (2022), and the blue circles are from H. Pan et al. (2023). The shaded areas are 1σ statistical uncertainties on the $\langle \log_{10}(M_{\rm HI})\rangle$.

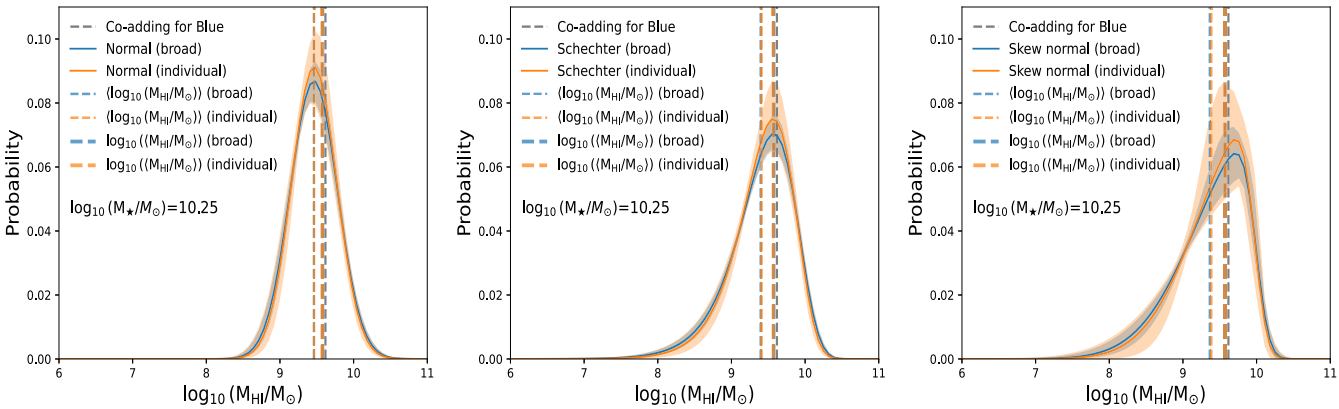

Figure 10. Conditional probability distribution of the H I mass on the stellar mass of $\log_{10}(M_\star/{\rm M}_\odot) = 10.25$ for blue galaxies at $0.25 < z < 0.5$. Three models (Normal, Schechter, Skew normal) are fit to the data from left to right panels. The blue and orange are the probability distributions for the broad and individual mass ranges, respectively. The thin and thick dashed lines are the $\langle \log_{10}(M_{\rm HI})\rangle$ and $\log_{10}(\langle M_{\rm HI}\rangle)$, respectively. The grey dashed line is the logarithmic of directly averaging $M_{\rm HI}$, labelled as 'Co-adding'.

The deviation between the SIMBA HIMF and the MIGHTEE conditional H I mass function (from our Schechter and Skew normal models) at the high H I mass end is notable, again indicating that SIMBA is likely overestimating the amount of H I gas in the massive galaxies. The overall (2–10 times) offset between the ALFALFA (and the MIGHTEE HIMF; A. A. Ponomareva et al. 2023 at $z = 0$) and the MIGHTEE HIMF at $0.25 < z < 0.5$ for the massive H I galaxies at $10 < \log_{10}(M_{\rm HI}/{\rm M}_\odot) < 10.5$ suggests a scenario of non-negligible evolution in their H I gas content. This offset is in reasonably good agreement with the finding in A. Bera et al. (2022) using the traditional stacking experiment at $z \sim 0.35$, indicating that massive galaxies at $z \sim 0$ have acquired a significant amount of H I over the past 4 Gyr, through either merger events or accretion from their surrounding CGM and IGM. This is also roughly consistent with the recent measurements of the H I mass function from intensity mapping (S. Paul et al. 2023) at $z \sim 0.32$ and the apparent mild evolution in the cosmic H I mass density (e.g. C. Péroux & J. C. Howk 2020).

We note that F. Sinigaglia et al. (2025) measured a notably higher HIMF than we do in this work, at a similar redshift. However, this is unsurprising considering that F. Sinigaglia et al. (2025) used the scaling relation between stellar mass and H I mass for star-forming galaxies derived from A. Bianchetti et al. (2025) for inferring the HIMF, as mentioned in Section 4.3. The A. Bianchetti et al. (2025) scaling relation is much steeper than we find here, and also steeper than that found by F. Sinigaglia et al. (2022) using the same data set. A. Bianchetti et al. (2025) discuss this in the appendix of their paper, and attribute the difference to the significantly more stringent definition of star-forming galaxies. This selection thus minimizes the contamination from galaxies significantly below the star-formation main sequence. However, as noted in section 2.1.2 in A. Bianchetti et al. (2025), by enforcing a symmetric scatter around the main sequence they remove around 25 per cent of the least star forming population, even if the colour selection criteria is satisfied. On the other hand, the GSMF used to convert the scaling relation to the HIMF in F. Sinigaglia et al. (2025) is from J. R. Weaver et al. (2023),

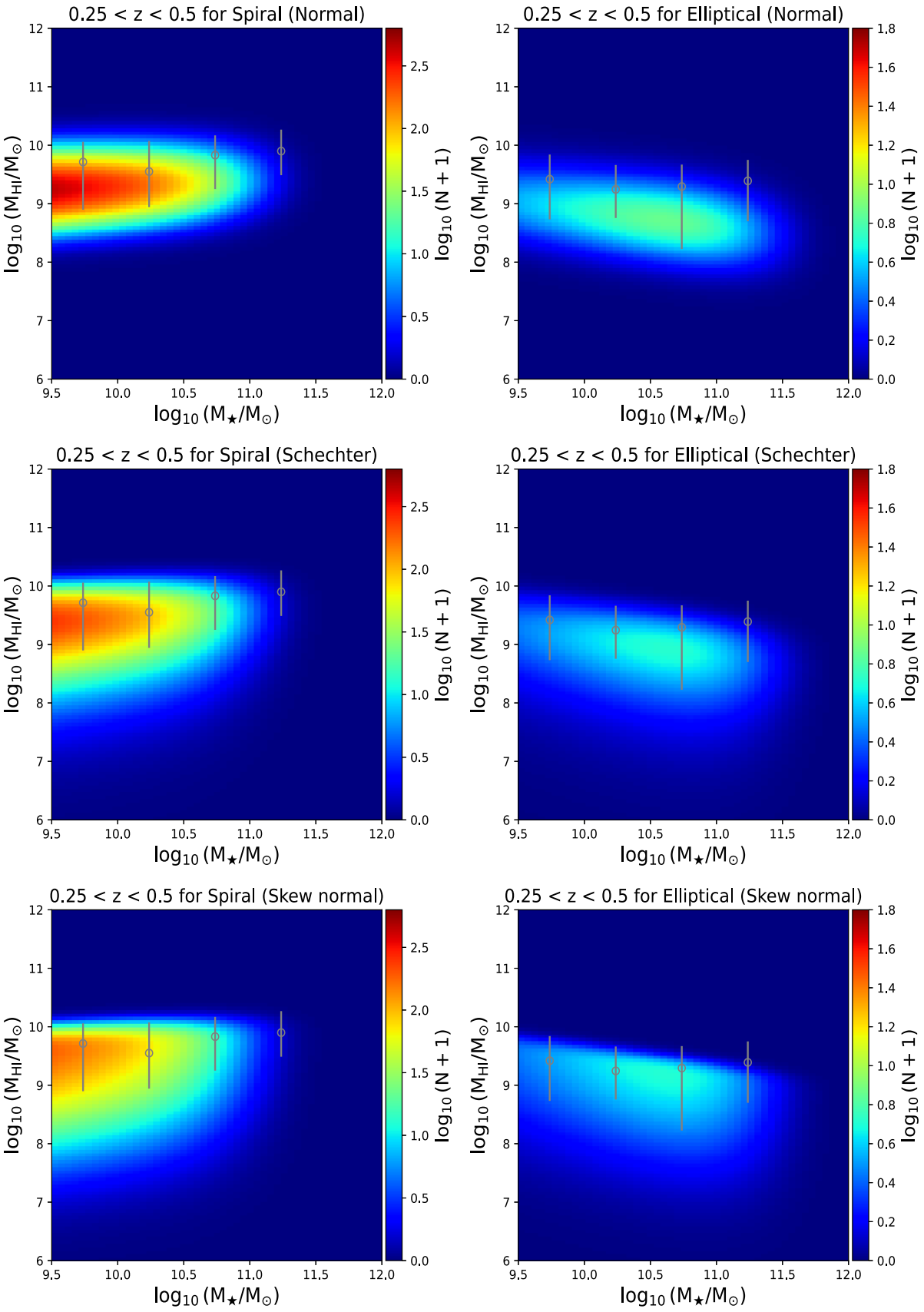

Figure 11. Bivariate distribution of H I mass and stellar mass for spiral (left) and elliptical (right) galaxies at $0.25 < z < 0.5$. Three models (Normal, Schechter, Skew normal) are used to fit the data from top to bottom panels. The grey circles with the error bars corresponds to the 16th, 50th, and 84th percentiles for the H I mass in four stellar mass bins from the SIMBA simulation (R. Davé et al. 2019). The corresponding posteriors are appended in Fig. C2.

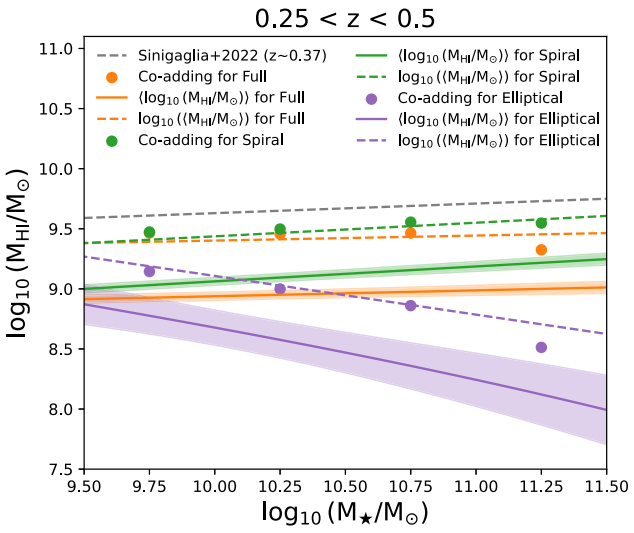

Figure 12. Best-fitting $M_{\rm H\,I} - M_\star$ scaling relation for the full sample, spiral, and elliptical galaxies with the Skew normal model, colour-coded by orange, green, and purple, respectively. The solid and dashed lines are the $\langle \log_{10}(M_{\rm H\,I})\rangle$ and $\log_{10}(\langle M_{\rm H\,I}\rangle)$, respectively. The solid dots are the logarithmic of directly averaging $M_{\rm H\,I}$, labelled as 'Co-adding'. The dashed grey line is from F. Sinigaglia et al. (2022).

who determine the star-forming GSMF from the purely colour-selected sample. As such the scaling relation from A. Bianchetti et al. (2025) combined with the GSMF of *all* star-forming galaxies results in a HIMF that is skewed to high values, compared to the HIMF we find in this paper. In this work, the sample used to determine the scaling relation is also that used to determine the GSMF that we use, as such they should result a HIMF that is less susceptible to possible biases in the mismatch of samples. We note that this is an important point for future studies, as a GSMF that is derived from a complete sample, and then used with an incomplete or mismatched sample used for determining the scaling relation, may lead to a bias in the predicted abundance of H I at high-stellar masses.

Although our sample is only complete at $\log_{10}(M_\star/{\rm M}_\odot) > 9.5$, it would require > 50 times more mass in H I than in stellar mass for galaxies below our stellar mass limit to contribute to the high H I mass to bring our results down and in agreement with the $z \sim 0$ HIMF, which would appear to be unlikely given the upper envelope in the $M_\star - M_{\rm H\,I}$ relation discussed in N. Maddox et al. (2015) and H. Pan et al. (2023).

The H I mass function for the massive galaxies with the preferred Schechter and Skew normal distributions peaks at $\log_{10}(M_{\rm H\,I}/{\rm M}_\odot) = 9.5 \sim 10$, which roughly corresponds to the knee of the H I mass function from ALFALFA, further demonstrating that the $\log_{10}(M_\star/{\rm M}_\odot) > 9.5$ galaxies trace the galaxies containing the largest amount of H I gas, albeit not necessarily the largest fraction of H I. The existence of red spiral galaxies across a wide H I mass range is also revealed by comparing the red and elliptical H I mass functions measured from the subsamples. The combined total HIMF from the red and blue subsamples is shown in the orange dotted line, and in line with the HIMF measured from the full sample in the orange solid line across a wide H I mass range. The discrepancy only increases towards the low-H I mass end where the statistical uncertainties are large as shown by the shaded areas.

At the highest mass end of $\log_{10}(M_{\rm H\,I}/{\rm M}_\odot) > 10.5$, the H I mass function measured using our symmetric Normal model shows the smallest deviation from the ALFALFA HIMF at $z = 0$, and would imply a minimal amount of evolution in the HIMF if it was correct. Indeed, work assuming a symmetric underlying distribution around a mean value (as widely conducted using traditional stacking techniques), would potentially lead to an incorrect measurement of H I distribution at the high-mass end. The fact that our results disfavour the symmetric underlying normal distribution demonstrates the importance of properly modelling the underlying distribution. Specifically, A. Chowdhury, N. Kanekar & J. N. Chengalur (2024) observed a strong evolution of the number density for high H I mass galaxies at $z \sim 1$, and they did not find a consistent evolution trend with A. Bera et al. (2022) using the similar approach of combining the *B*-band luminosity function and the scaling relation between the H I mass and *B*-band luminosity ($M_{\rm B}$) of star-forming galaxies at $z \sim 0.35$. A. Chowdhury et al. (2024) suspected that this apparent contradiction is due to the differing net gas accretion rate for high star-forming galaxies between $0.35 < z < 1$ and $0 < z < 0.35$ and the influence of the cosmic variance on the measurement of the $M_{\rm H\,I} - M_{\rm B}$ relation over a small cosmic volume. However, the assumption of using the symmetrical H I scatter at $z \sim 1$ may also be an important limiting factor for them to construct a consistent HIMF given the comparison between the Normal, Schechter, and Skew normal for the H I mass function on the high-mass end in Fig. 13. We append the best-fitting conditional H I mass function with Schechter and Skew normal models in Table D1.

5 CONCLUSIONS

We implement a Bayesian technique, developed from our previous work (H. Pan et al. 2021, 2023), to the MIGHTEE DR1 images for measuring the underlying $M_{\rm H\,I} - M_\star$ scaling relation by using the information from the DEVILS spectroscopic catalogue at $0.25 < z < 0.5$, while taking into account the intrinsic H I distribution as a function of the stellar mass. Our results are highlighted as follows:

(i) We measure the bivariate distribution of H I mass and stellar mass of massive galaxies down to $\log_{10}(M_\star/{\rm M}_\odot) = 9.5$ at $0.25 < z < 0.5$ for the full galaxy sample, with three conditional probability distributions of H I mass (Normal, Schechter, and Skew normal). The asymmetric H I distributions are strongly preferred by our data.

(ii) We differentiate the concepts of the average of the logarithmic H I mass, i.e. $\langle \log_{10}(M_{\rm H\,I})\rangle$, and the logarithmic average of the H I mass, i.e. $\log_{10}(\langle M_{\rm H\,I}\rangle)$, to clarify the statistical confusions in the stacking approaches, and find that the difference between $\langle \log_{10}(M_{\rm H\,I})\rangle$ and $\log_{10}(\langle M_{\rm H\,I}\rangle)$ is non-trivial with 0.2–0.3 dex for normal and Schechter models, and ~0.5 dex for the Skew normal.

(iii) We observe shallow slopes in the underlying $M_{\rm H\,I} - M_\star$ scaling relation, suggesting the presence of an upper H I mass limit beyond which a galaxy can no longer accrete or retain further H I gas, and find tentative evidence of mild negative evolution for the H I distribution in massive galaxies at $z < 0.5$ when compared to local $M_{\rm H\,I} - M_\star$ relation.

(iv) By studying the colour dependence of the $M_{\rm H\,I} - M_\star$ relation, we find that the Schechter and Skew normal profiles provide the best description of the conditional H I mass distribution for blue galaxies, and the Normal profile is sufficient for describing the H I destribution of red galaxies becasue of their small sample size in our present catalogue. This trend is also true for the spiral and ellipical subsamples due to the strong colour–morphology correlation of galaxies.

(v) The massive blue (or spiral) galaxies are tightly clustered in the stellar mass bins of $9.5 < \log_{10}(M_\star/{\rm M}_\odot) < 10.5$ and relatively high

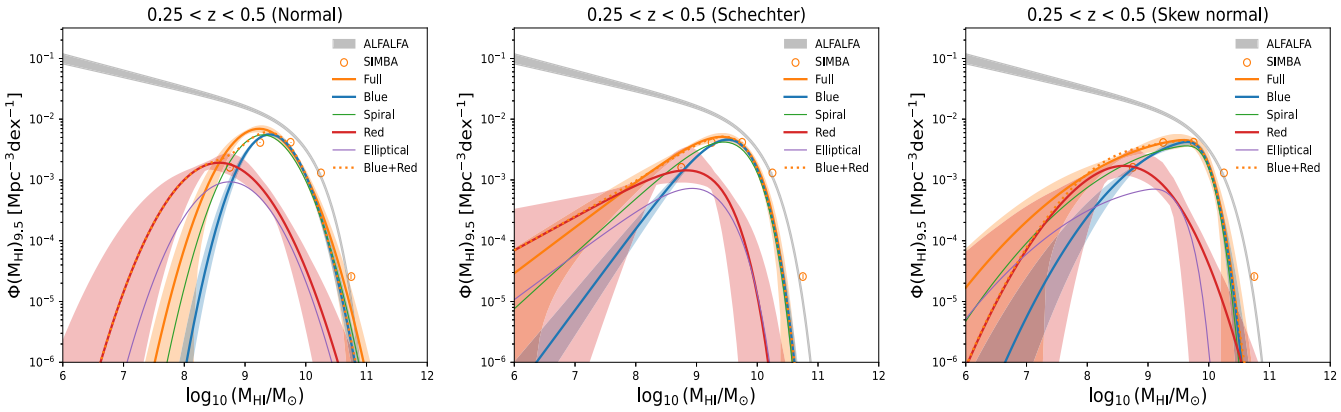

Figure 13. Conditional H I mass function for all samples at $0.25 < z < 0.5$. Three models (Normal, Schechter, Skew normal) are fit to the data from left to right panels. The blue, red, green, and purple lines are for the blue, red, spiral, and elliptical subsamples while the corresponding shaded areas are 1σ statistical uncertainties from our Bayesian modelling. The orange lines are for the full sample with uncertainties derived from combining our modelling and error propagation from the GSMF (A. Hashemizadeh et al. 2022). Note that the shaded areas for spiral and elliptical subsamples are omitted for simplicity. The grey shaded area is the 1σ band of the H I mass function at $z < 0.06$ from the ALFALFA survey (M. G. Jones et al. 2018). The orange circles are the H I mass function of $9.5 < \log_{10}(M_\star/\mathrm{M}_\odot)$ galaxies from the SIMBA simulation (R. Davé et al. 2019).

H I mass range of $9 < \log_{10}(M_{\mathrm{H\,I}}/\mathrm{M}_\odot) < 10$ while the massive red (or elliptical) galaxies instead sit broadly in the intermediate stellar mass range of $9.5 < \log_{10}(M_\star/\mathrm{M}_\odot) < 11.5$ and the H I mass range of $7.5 < \log_{10}(M_{\mathrm{H\,I}}/\mathrm{M}_\odot) < 9.5$.

(vi) The H I masses of massive blue and spiral galaxies are positively correlated with their stellar masses. Red galaxies follow a similar trend, largely due to the presence of a significant fraction of red disc galaxies. In contrast, the H I mass appears to be anticorrelated with stellar mass for ellipticals, suggesting that more massive elliptical galaxies are more efficient at consuming or losing their H I gas.

We also present the H I mass function for $\log_{10}(M_\star/\mathrm{M}_\odot) > 9.5$ galaxies and find that this conditional HIMF is several times lower than the HIMF for the general galaxy population from ALFALFA at the highest H I mass end, indicating a mild or moderate evolutionary picture for the extremely H I rich galaxies observed at low redshift. Although we note that understanding the environmental effects on the measured HIMF will be important for future work with larger samples (e.g. F. Sinigaglia et al. 2024).

In conclusion, we present the Bayesian stacking technique that is capable of probing the underlying H I distribution at the distant Universe, and measure the $M_{\mathrm{H\,I}} - M_\star$ relation above or below the detection threshold in a unified way while modelling the scatter self-consistently within the same procedure without binning the data sets. This technique allows us to put tighter constraints on the galaxy formation and evolution models compared to the traditional stacking approach. The $\log_{10}(\langle M_{\mathrm{H\,I}}\rangle)$, i.e. traditional stacking, is more robust at picking out the peak of the distribution for an asymmetrical underlying H I distribution skewed towards lower mass galaxies and is less susceptible to the form of the underlying distribution compared to $\langle \log_{10}(M_{\mathrm{H\,I}})\rangle$.

ACKNOWLEDGEMENTS

The MeerKAT telescope is operated by the South African Radio Astronomy Observatory, which is a facility of the National Research Foundation, an agency of the Department of Science and Innovation. We acknowledge use of the IDIA data intensive research cloud for data processing. The IDIA is a South African university partnership involving the University of Cape Town, the University of Pretoria, and the University of the Western Cape. The authors acknowledge the Centre for High Performance Computing (CHPC), South Africa, for providing computational resources to this research project.

We acknowledge the use of the ilifu cloud computing facility – www.ilifu.ac.za, a partnership between the University of Cape Town, the University of the Western Cape, the University of Stellenbosch, Sol Plaatje University, the Cape Peninsula University of Technology, and the South African Radio Astronomy Observatory. The ilifu facility is supported by contributions from IDIA and the Computational Biology division at UCT and the Data Intensive Research Initiative of South Africa (DIRISA).

We thank the anonymous referee for their helpful comments that have improved this paper. HP, MJJ, IH, and TY acknowledge support from a UKRI Frontiers Research Grant [EP/X026639/1], which was selected by the the European Research Council. MJJ, IH, and MGS acknowledge support from the South African Radio Astronomy Observatory (SARAO) towards this research (www.sarao.ac.za). MJJ acknowledges generous support from the Hintze Family Charitable Foundation through the Oxford Hintze Centre for Astrophysical Surveys and the UK Science and Technology Facilities Council [ST/S000488/1]. HP acknowledges support from National Key R&D Program of China No. 2022YFA1602904, Guizhou Provincial Science and Technology Projects (No. QKHFQ[2023]003, No. QKHFQ[2024]001, No. QKHPTRC-ZDSYS[2023]003), and Guizhou Province High-level Talent Program (No. QKHPTRCGCC[2022]003-1).

For the purpose of Open Access, the author has applied a CC BY public copyright licence to any Author Accepted Manuscript version arising from this submission.

DATA AVAILABILITY

The MIGHTEE DR1 data are available in I. Heywood et al. (2024).

REFERENCES

Aihara H. et al., 2018, PASJ, 70, S4
Aihara H. et al., 2019, PASJ, 71, 114
Bamford S. P. et al., 2009, MNRAS, 393, 1324

Barnes D. G. et al., 2001, MNRAS, 322, 486
Bera A., Kanekar N., Chengalur J. N., Bagla J. S., 2022, ApJ, 940, L10
Bianchetti A. et al., 2025, ApJ, 982, 82
Blyth S. et al., 2016, in MeerKAT Science: On the Pathway to the SKA. SISSA, Italy, p. 4
Buchner J. et al., 2014, A&A, 564, A125
Capak P. et al., 2007, ApJS, 172, 99
Catinella B. et al., 2010, MNRAS, 403, 683
Chowdhury A., Kanekar N., Chengalur J. N., 2024, ApJ, 966, L39
Cuillandre J.-C. J. et al., 2012, in Peck A. B., Seaman R. L., Comeron F., eds, Proc. SPIE Conf. Ser., Vol. 8448, Observatory Operations: Strategies, Processes, and Systems IV. SPIE, Bellingham, p. 84480M
Davé R., Anglés-Alcázar D., Narayanan D., Li Q., Rafieferantsoa M. H., Appleby S., 2019, MNRAS, 486, 2827
Davies L. J. M. et al., 2018, MNRAS, 480, 768
Davies L. J. M. et al., 2021, MNRAS, 506, 256
Delhaize J., Meyer M. J., Staveley-Smith L., Boyle B. J., 2013, MNRAS, 433, 1398
Elson E., Glowacki M., Davé R., 2023, New Astron., 99, 101 964
Fernández X. et al., 2016, ApJ, 824, L1
Feroz F., Hobson M. P., Bridges M., 2009, MNRAS, 398, 1601
Giovanelli R. et al., 2005, AJ, 130, 2598
Hashemizadeh A. et al., 2021, MNRAS, 505, 136
Hashemizadeh A. et al., 2022, MNRAS, 515, 1175
Healy J., Blyth S.-L., Elson E., van Driel W., Butcher Z., Schneider S., Lehnert M. D., Minchin R., 2019, MNRAS, 487, 4901
Heywood I. et al., 2024, MNRAS, 534, 76
Huang S., Haynes M. P., Giovanelli R., Brinchmann J., 2012, ApJ, 756, 113
Jarvis M. et al., 2016, in MeerKAT Science: On the Pathway to the SKA. SISSA, Italy, p. 6
Jarvis M. J. et al., 2024, MNRAS, 529, 3484
Jarvis M. J. et al., 2025, MNRAS, 544, 193
Jonas J., Team MeerKAT, 2016, in MeerKAT Science: On the Pathway to the SKA. SISSA, Italy, p. 1
Jones M. G., Haynes M. P., Giovanelli R., Moorman C., 2018, MNRAS, 477, 2
Kazemi-Moridani A. et al., 2024, ApJ, 981, 208
Kleiner D., Pimbblet K. A., Heath Jones D., Koribalski B. S., Serra P., 2017, MNRAS, 466, 4692
Lopes P. A. A., Rembold S. B., Ribeiro A. L. B., Nascimento R. S., Vajgel B., 2016, MNRAS, 461, 2559
Maddox N., Hess K. M., Obreschkow D., Jarvis M. J., Blyth S. L., 2015, MNRAS, 447, 1610
Maddox N. et al., 2021, A&A, 646, A35
Mahajan S. et al., 2019, MNRAS, 491, 398
Masters K. L. et al., 2010, MNRAS, 405, 783
McCracken H. J. et al., 2012, A&A, 544, A156
Meyer M., Robotham A., Obreschkow D., Westmeier T., Duffy A. R., Staveley-Smith L., 2017, Publ. Astron. Soc. Aust., 34, e052
Nan R. et al., 2011, Int. J. Mod. Phys. D, 20, 989
Pan H., Jarvis M. J., Allison J. R., Heywood I., Santos M. G., Maddox N., Frank B. S., Kang X., 2020, MNRAS, 491, 1227
Pan H., Jarvis M. J., Ponomareva A. A., Santos M. G., Allison J. R., Maddox N., Frank B. S., 2021, MNRAS, 508, 1897
Pan H. et al., 2023, MNRAS, 525, 256
Pan H. et al., 2024, MNRAS, 534, 202
Parkash V., Brown M. J. I., Jarrett T. H., Bonne N. J., 2018, ApJ, 864, 40
Paul S., Santos M. G., Chen Z., Wolz L., 2023, preprint (arXiv:2301.11943)
Péroux C., Howk J. C., 2020, ARA&A, 58, 363
Ponomareva A. A. et al., 2021, MNRAS, 508, 1195
Ponomareva A. A. et al., 2023, MNRAS, 522, 5308
Rodríguez-Puebla A., Calette A., Avila-Reese V., Rodriguez-Gomez V., Huertas-Company M., 2020, Publ. Astron. Soc. Aust., 37, e024
Saintonge A., Catinella B., 2022, ARA&A, 60, 319
Sales L. V., Navarro J. F., Theuns T., Schaye J., White S. D. M., Frenk C. S., Crain R. A., Vecchia C. D., 2012, MNRAS, 423, 1544
Schawinski K. et al., 2014, MNRAS, 440, 889
Sinigaglia F. et al., 2022, ApJ, 935, L13
Sinigaglia F. et al., 2024, MNRAS, 529, 4192
Sinigaglia F., Bianchetti A., Rodighiero G., Mayer L., Dessauges-Zavadsky M., Elson E., Vaccari M., Jarvis M. J., 2025, preprint (arXiv:2506.11280)
Thorne J. E. et al., 2021, MNRAS, 505, 540
Wang L. et al., 2022, MNRAS, 516, 2337
Weaver J. R. et al., 2023, A&A, 677, A184
Xi H., Peng B., Staveley-Smith L., For B.-Q., Liu B., Ding D., 2024, ApJS, 274, 18
Zhang C.-P. et al., 2024, Sci. China-Phys. Mech. Astron., 67, 219511
Zhou S., Li C., Hao C.-N., Guo R., Mo H., Xia X., 2021, ApJ, 916, 38

APPENDIX A: MEASURED H I MASS

We used equation (1) to calculate the intrinsic H I fluxes with assumed H I masses driven from the underlying H I mass and stellar mass relation as the majority of our extracted fluxes are below the detection threshold at the redshift range of $0.25 < z < 0.5$. However, in this section, we use equation (1) to measure the individual H I masses directly from the extracted fluxes to intuitively understand the distribution of the measured H I mass of $M_{\rm H\,I}^{\rm m}$, although we note that many of these measurements could be negative due to the presence of low-SNR sources. We show the measured H I mass ($M_{\rm H\,I}^{\rm m}$) distribution in Fig. A1, which can be turned into the SNR distribution in Fig. 5 after the noise normalization. We also show the bivariate distribution of the $M_{\rm H\,I}^{\rm m}$ and $M_\star$ in Fig. A2, which corresponds to the best-fitting bivariate distribution of the intrinsic H I mass and stellar mass in Fig. 6.

The aperture size for our flux extraction is 16 arcsec, which is slightly lower than the typical synthesized beam size for the robust = 0.5 (r0.5) H I spectral cube at the redshift range of $0.25 < z < 0.5$. This choice is to reduce the influence from the difference between the synthesized beam and the corresponding Gaussian model when we use the integral over the source to measure the H I flux. We plot the ratio of the integral to peak flux as a function of the aperture size for the synthesized beam and the corresponding Gaussian model in Fig. A3 for the maser discovered by M. J. Jarvis et al. (2024), and use the vertical line to mark the size of 16 arcsec. At this size, the fraction difference between the synthesized beam and the corresponding Gaussian model is less than ∼2 per cent for both r0.5 and r0.0 H I

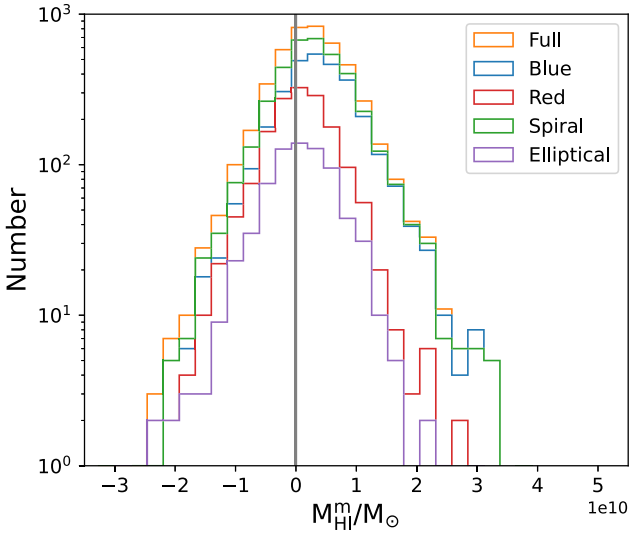

Figure A1. Measured H I mass distribution from MIGHTEE DR1 data at $0.25 < z < 0.5$.

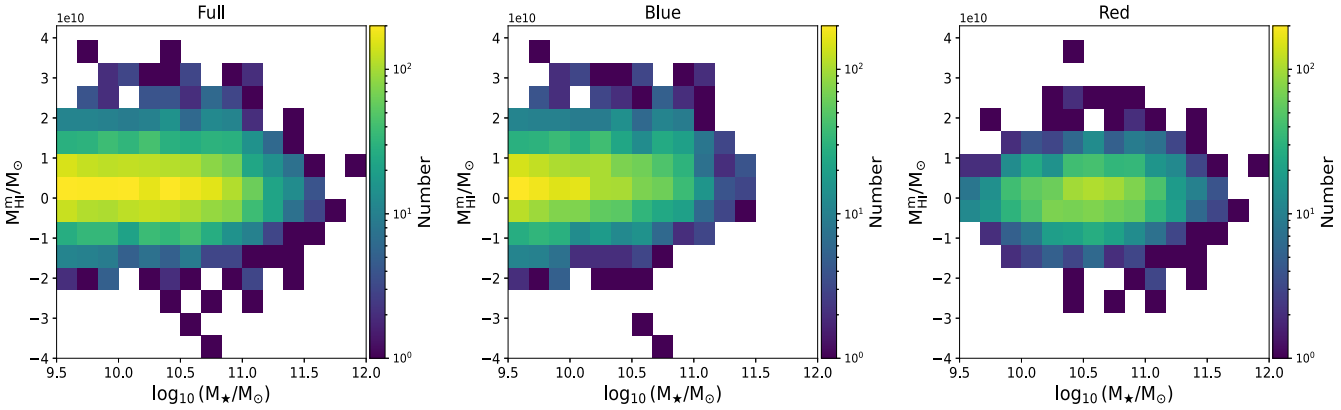

Figure A2. Bivariate distribution of the measured H I mass and stellar mass for the full (left), blue (middle), and red (right) galaxies at $0.25 < z < 0.5$.

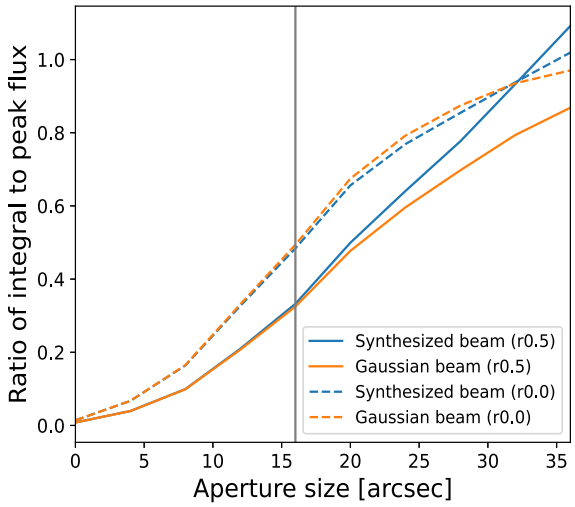

Figure A3. Ratio of the integral to peak flux for the discovered maser by M. J. Jarvis et al. (2024). The blue and orange lines are the synthesized beam and the corresponding Gaussian model. The solid and dashed lines are for the r0.5 and r0.0 H I spectral cubes, respectively.

cubes, and it increases gradually when the aperture size is larger. To also minimize the noise influence, we chose the r0.5 H I spectral cube to extract the H I fluxes, and measure the H I masses based on them.

APPENDIX B: INJECTION AND RECOVERY

Our approach for measuring the H I mass and stellar mass relation relies on assuming the Gaussianity of the noise distribution in the H I spectral cube. However, in practice the real noise behaviour deviates from the perfect Gaussian distribution. To examine the influence of the real noise on our approach, we inject fake sources with known $M_{\rm H\,I} - M_{\star}$ relation and try to reconstruct this relation to verify if our approach is immune to the minor non-Gaussian noise behaviour.

The input $M_{\rm H\,I} - M_{\star}$ relation follows our Model A with parameters a, b, and $\sigma_{\rm H\,I}$ of 0.21, 9.37, and 0.47, which are in the range of typical values for the $M_{\rm H\,I} - M_{\star}$ relation of blue or star-forming galaxies. We use this relation to generate the H I masses, and convert them into fluxes based on their stellar masses and redshifts. We then inject the flux for each fake source into a random position surrounding the real source (over a distance range of 5–10 beams), and we repeat this process for 100 times to get a high statistical significance on the agreement between the input parameters and reconstructed ones. This whole process is to further verify that our approach is not influenced by the random sampling, which in turn proves that the noise surrounding the source in our data is indeed well-behaved. We also simulate a data cube with Gaussian background noise for conducting the same injections as a reference.

We show the histograms for the recovered parameters in Fig. B1. The blue and orange lines correspond to the results reconstructed from the real background noise and fake Gaussian noise, respectively. The grey vertical lines are the input values for our assumed model. For all three parameters in both cases, the median reconstructed values are in great agreement with the input values, with a fraction difference of <1 per cent. The spread widths are on a scale of $\sim$0.02 as expected from our Bayesian modelling. The fraction difference between the Real noise and Gaussian noise on our approach is also less than 1 per cent for the median reconstructed values, demonstrating that the influence of the real noise distribution (slightly deviated from the perfect Gaussian) on the accuracy of our approach for measuring the $M_{\rm H\,I} - M_{\star}$ relation is minimal.

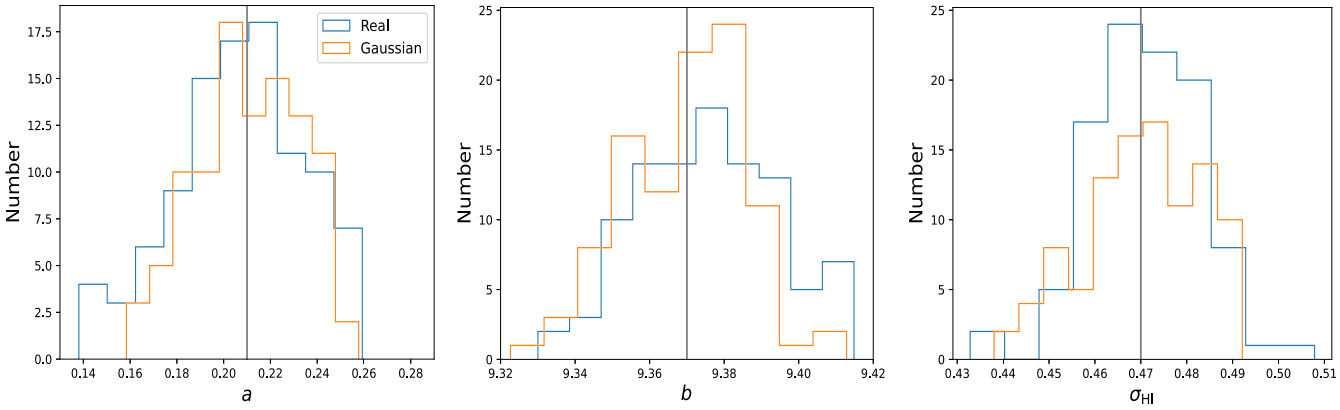

Figure B1. Reconstructed parameters of a, b, $\sigma_{\rm H\,I}$ for the input H I mass and stellar mass relation from left to right panels. The blue and orange lines correspond to the results derived from real and simulated Gaussian background noise, respectively. The grey vertical lines are the input values for an assumed $M_{\rm H\,I} - M_\star$ relation model.

APPENDIX C: POSTERIORS

The posterior distributions of modelling the H I mass and stellar mass relation at $0.25 < z < 0.5$ for the blue and red galaxies are shown in Fig. C1, and for the spiral and elliptical galaxies in Fig. C2, respectively.

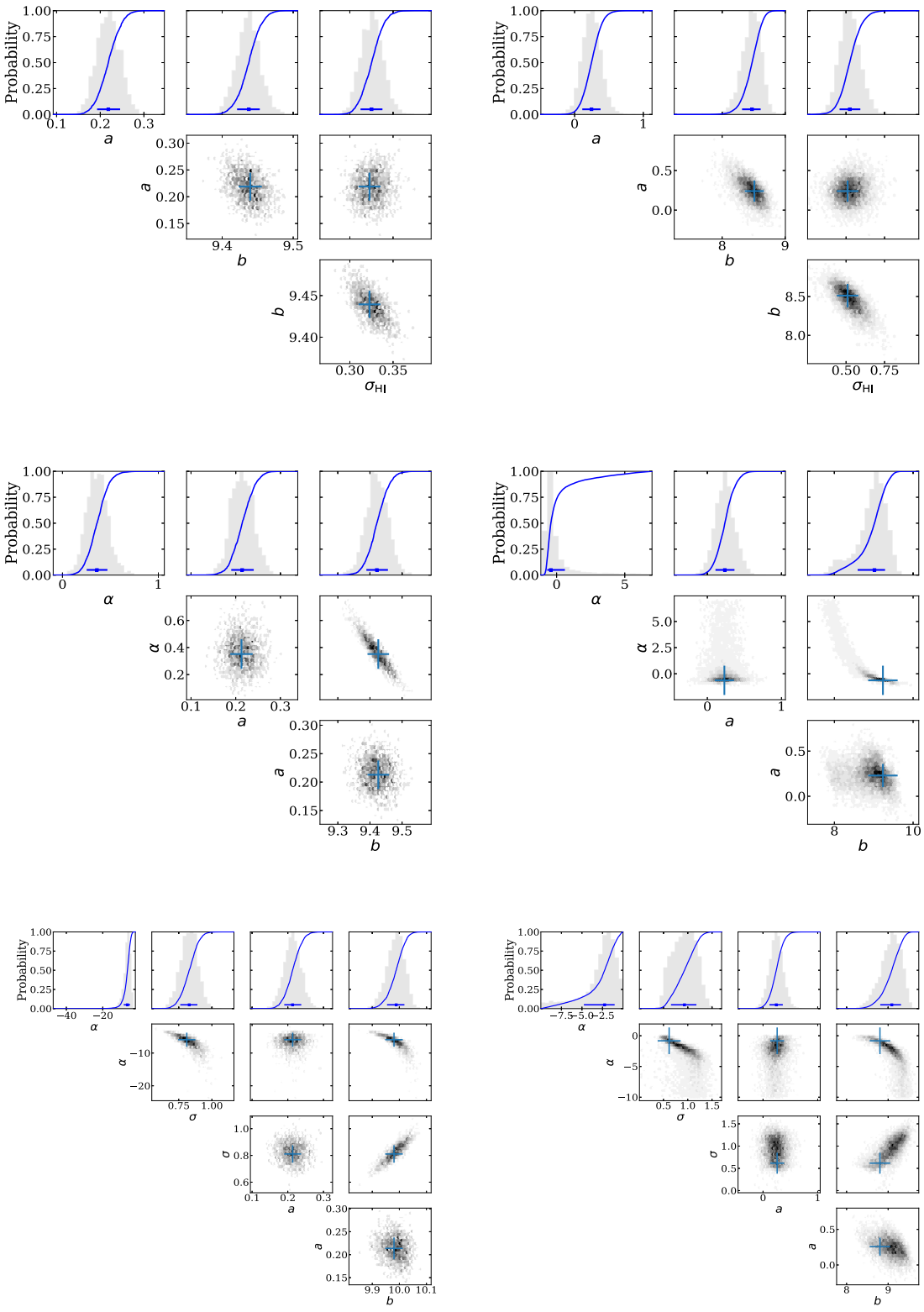

Figure C1. Posterior distributions for three models (Normal, Schechter, Skew normal) of the H I mass and stellar mass relation at $0.25 < z < 0.5$ from top to bottom panels. The left and right panels are for the blue and red galaxies, respectively. The grey histograms represent the marginal posterior probabilities (1D or 2D), while the blue curves indicate the cumulative distributions. In the 2D posterior plots, the blue crosses mark the parameter set with the maximum likelihood, and the 1σ error bars are estimated from the 1D marginal posterior distributions.

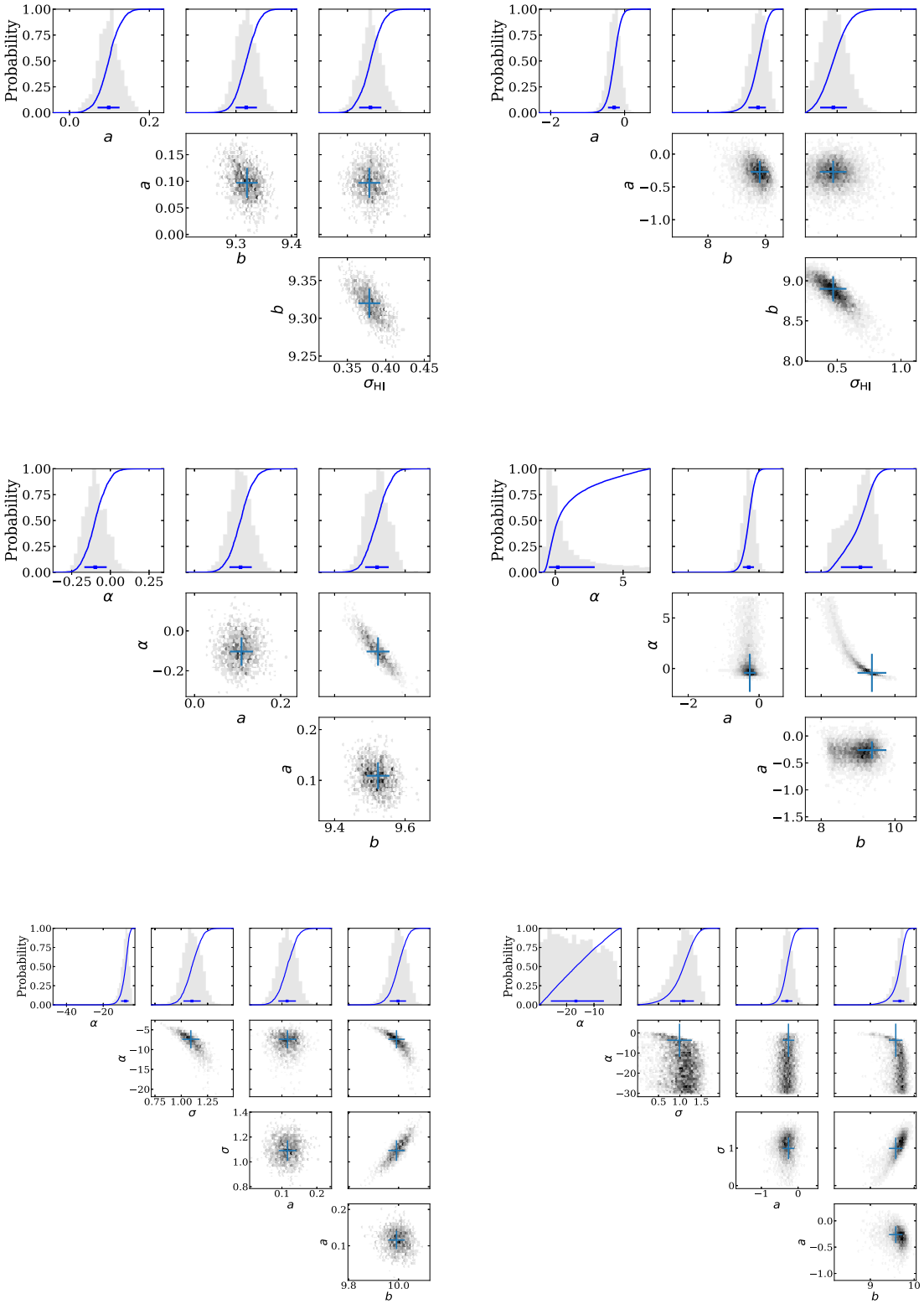

Figure C2. The same as the caption of Fig. C1, except that the left and right panels are for the spiral and elliptical galaxies, respectively.

APPENDIX D: BEST-FITTING CONDITIONAL HIMF

We list the best-fitting conditional H I mass functions with Schechter and Skew normal models in Table D1 for reference and ease of comparison for future work.

Table D1. Best-fitting conditional H I mass functions with Schechter and Skew normal models for the full galaxy sample, blue, red, spiral, elliptical subsamples at $0.25 < z < 0.5$. The conditional HIMF for the Full (Blue+Red) is the sum of the conditional HIMFs for the Blue and Red subsamples, which has better performance than for the Full sample, particularly at the low-mass end, due to more accurate modelling.

$\log_{10}(M_{\rm H\,I}/M_\odot)$	$\Phi(\mathrm{M_{H\,I}})_{9.5} h_{70}^{-3}$ [$\mathrm{Mpc^{-3}dex^{-1}}$]					
	Full	Blue	Spiral	Red	Elliptical	Full (Blue+Red)
			Schechter			
6.0	2.90×10^{-5}	–	8.00×10^{-6}	6.90×10^{-5}	1.10×10^{-5}	7.00×10^{-5}
6.2	4.10×10^{-5}	1.00×10^{-6}	1.20×10^{-5}	8.90×10^{-5}	1.50×10^{-5}	9.00×10^{-5}
6.4	5.80×10^{-5}	1.00×10^{-6}	1.80×10^{-5}	1.15×10^{-4}	2.10×10^{-5}	1.16×10^{-4}
6.6	8.30×10^{-5}	2.00×10^{-6}	2.70×10^{-5}	1.48×10^{-4}	3.00×10^{-5}	1.50×10^{-4}
6.8	1.17×10^{-4}	4.00×10^{-6}	4.10×10^{-5}	1.91×10^{-4}	4.20×10^{-5}	1.95×10^{-4}
7.0	1.65×10^{-4}	7.00×10^{-6}	6.20×10^{-5}	2.45×10^{-4}	5.80×10^{-5}	2.52×10^{-4}
7.2	2.33×10^{-4}	1.30×10^{-5}	9.40×10^{-5}	3.14×10^{-4}	8.20×10^{-5}	3.28×10^{-4}
7.4	3.28×10^{-4}	2.50×10^{-5}	1.42×10^{-4}	4.02×10^{-4}	1.14×10^{-4}	4.27×10^{-4}
7.6	4.62×10^{-4}	4.60×10^{-5}	2.15×10^{-4}	5.11×10^{-4}	1.58×10^{-4}	5.57×10^{-4}
7.8	6.50×10^{-4}	8.50×10^{-5}	3.25×10^{-4}	6.46×10^{-4}	2.17×10^{-4}	7.31×10^{-4}
8.0	9.09×10^{-4}	1.56×10^{-4}	4.88×10^{-4}	8.07×10^{-4}	2.95×10^{-4}	9.63×10^{-4}
8.2	1.27×10^{-3}	2.84×10^{-4}	7.28×10^{-4}	9.91×10^{-4}	3.92×10^{-4}	1.27×10^{-3}
8.4	1.74×10^{-3}	5.08×10^{-4}	1.08×10^{-3}	1.18×10^{-3}	5.05×10^{-4}	1.69×10^{-3}
8.6	2.36×10^{-3}	8.90×10^{-4}	1.56×10^{-3}	1.35×10^{-3}	6.20×10^{-4}	2.24×10^{-3}
8.8	3.12×10^{-3}	1.50×10^{-3}	2.20×10^{-3}	1.44×10^{-3}	7.07×10^{-4}	2.94×10^{-3}
9.0	3.96×10^{-3}	2.39×10^{-3}	2.96×10^{-3}	1.38×10^{-3}	7.20×10^{-4}	3.77×10^{-3}
9.2	4.73×10^{-3}	3.49×10^{-3}	3.72×10^{-3}	1.12×10^{-3}	6.22×10^{-4}	4.61×10^{-3}
9.4	5.11×10^{-3}	4.41×10^{-3}	4.18×10^{-3}	7.15×10^{-4}	4.28×10^{-4}	5.13×10^{-3}
9.6	4.72×10^{-3}	4.49×10^{-3}	3.94×10^{-3}	3.22×10^{-4}	2.17×10^{-4}	4.81×10^{-3}
9.8	3.40×10^{-3}	3.29×10^{-3}	2.82×10^{-3}	8.90×10^{-5}	7.20×10^{-5}	3.38×10^{-3}
10.0	1.65×10^{-3}	1.50×10^{-3}	1.31×10^{-3}	1.30×10^{-5}	1.30×10^{-5}	1.51×10^{-3}
10.2	4.29×10^{-4}	3.56×10^{-4}	3.15×10^{-4}	1.00×10^{-6}	1.00×10^{-6}	3.57×10^{-4}
10.4	4.20×10^{-5}	3.70×10^{-5}	2.80×10^{-5}	–	–	3.70×10^{-5}
10.6	1.00×10^{-6}	1.00×10^{-6}	1.00×10^{-6}	–	–	1.00×10^{-6}
			Skew normal			
6.0	1.70×10^{-5}	–	5.00×10^{-6}	1.00×10^{-6}	5.00×10^{-6}	1.00×10^{-6}
6.2	3.00×10^{-5}	–	9.00×10^{-6}	2.00×10^{-6}	9.00×10^{-6}	2.00×10^{-6}
6.4	5.00×10^{-5}	–	1.70×10^{-5}	6.00×10^{-6}	1.50×10^{-5}	6.00×10^{-6}
6.6	8.30×10^{-5}	1.00×10^{-6}	3.10×10^{-5}	1.50×10^{-5}	2.50×10^{-5}	1.60×10^{-5}
6.8	1.33×10^{-4}	2.00×10^{-6}	5.40×10^{-5}	3.40×10^{-5}	3.90×10^{-5}	3.60×10^{-5}
7.0	2.06×10^{-4}	6.00×10^{-6}	9.20×10^{-5}	7.10×10^{-5}	6.00×10^{-5}	7.70×10^{-5}
7.2	3.12×10^{-4}	1.30×10^{-5}	1.49×10^{-4}	1.41×10^{-4}	8.90×10^{-5}	1.54×10^{-4}
7.4	4.59×10^{-4}	3.00×10^{-5}	2.35×10^{-4}	2.58×10^{-4}	1.28×10^{-4}	2.88×10^{-4}
7.6	6.55×10^{-4}	6.50×10^{-5}	3.58×10^{-4}	4.39×10^{-4}	1.77×10^{-4}	5.04×10^{-4}
7.8	9.07×10^{-4}	1.31×10^{-4}	5.26×10^{-4}	6.93×10^{-4}	2.38×10^{-4}	8.24×10^{-4}
8.0	1.22×10^{-3}	2.47×10^{-4}	7.48×10^{-4}	1.01×10^{-3}	3.09×10^{-4}	1.25×10^{-3}
8.2	1.60×10^{-3}	4.39×10^{-4}	1.03×10^{-3}	1.34×10^{-3}	3.88×10^{-4}	1.77×10^{-3}
8.4	2.03×10^{-3}	7.32×10^{-4}	1.37×10^{-3}	1.60×10^{-3}	4.72×10^{-4}	2.33×10^{-3}
8.6	2.51×10^{-3}	1.15×10^{-3}	1.75×10^{-3}	1.71×10^{-3}	5.55×10^{-4}	2.85×10^{-3}
8.8	3.00×10^{-3}	1.69×10^{-3}	2.17×10^{-3}	1.60×10^{-3}	6.32×10^{-4}	3.29×10^{-3}
9.0	3.50×10^{-3}	2.34×10^{-3}	2.61×10^{-3}	1.30×10^{-3}	6.94×10^{-4}	3.64×10^{-3}
9.2	3.95×10^{-3}	3.04×10^{-3}	3.02×10^{-3}	9.11×10^{-4}	6.90×10^{-4}	3.95×10^{-3}
9.4	4.34×10^{-3}	3.71×10^{-3}	3.38×10^{-3}	5.43×10^{-4}	5.15×10^{-4}	4.25×10^{-3}
9.6	4.53×10^{-3}	4.20×10^{-3}	3.63×10^{-3}	2.73×10^{-4}	2.41×10^{-4}	4.47×10^{-3}
9.8	3.85×10^{-3}	3.72×10^{-3}	3.28×10^{-3}	1.15×10^{-4}	4.80×10^{-5}	3.83×10^{-3}
10.0	1.84×10^{-3}	1.69×10^{-3}	1.57×10^{-3}	4.10×10^{-5}	2.00×10^{-6}	1.73×10^{-3}
10.2	3.43×10^{-4}	2.89×10^{-4}	2.36×10^{-4}	1.20×10^{-5}	–	3.01×10^{-4}
10.4	2.00×10^{-5}	1.60×10^{-5}	8.00×10^{-6}	3.00×10^{-6}	–	1.90×10^{-5}
10.6	–	–	–	1.00×10^{-6}	–	1.00×10^{-6}

This paper has been typeset from a TEX/LATEX file prepared by the author.